



1  
2                   DOCTORAL THESIS

---

3  
4       Optimisation studies and background  
5       estimation in searches for the supersymmetric  
6       partner of the top quark in all-hadronic final  
7       states with the ATLAS Detector at the LHC

---

8  
9                   *A thesis submitted in fulfillment of the requirements*  
10                  *for the degree of Doctor of Philosophy*

11                  *in the*

12                  Experimental Particle Physics Research Group  
13                  School of Mathematical and Physical Sciences

14                  *Author:*  
15                  Fabrizio MIANO

Supervisor:  
Dr. Fabrizio SALVATORE

16                  14th November 2017

Dedicated to my family.

*Have no fear for atomic energy  
'cause none of them can stop the  
time*

17

---

Robert Nesta Marley

18

## *Acknowledgments*

- 19 Thanks to every single thing that went wrong. It made me stronger.

## *Declaration*

21 I, Fabrizio MIANO, hereby declare that this thesis, titled, "Optimisation studies and back-  
22 ground estimation in searches for the supersymmetric partner of the top quark in all-  
23 hadronic final states with the ATLAS Detector at the LHC" has not been and will not be,  
24 submitted in whole or in part to another University for the award of any other degree.

25 *Brighton, June 2018*

University of Sussex  
School of Mathematical and Physical Sciences  
Experimental Particle Physics Research Group

# Doctoral Thesis

31  
32 Optimisation studies and background estimation in searches for  
33 the supersymmetric partner of the top quark in all-hadronic final  
34 states with the ATLAS Detector at the LHC

36 by Fabrizio Miano

## *Abstract*

38 This thesis presents searches for supersymmetry in  $\sqrt{s} = 13$  TeV proton-proton collisions  
39 at the LHC using data collected by the ATLAS detector in 2015, 2016 and 2017. Events  
40 with 4 or more jets and missing transverse energy were selected. Kinematic variables were  
41 investigated and optimisations were performed to increase the sensitivity to supersym-  
42 metric signals. Standard Model backgrounds were estimated by means of Monte Carlo  
43 simulations and data-driven techniques. Before analysing the data in the blinded signal  
44 regions the agreement between data and background predictions and the extrapolations  
45 from control and validation regions to signal regions were validated. The analysis yiel-  
46 ded no significant excess in any of the analyses performed. Therefore limits were set and  
47 the results were interpreted as lower bounds on the masses of supersymmetric particles  
48 in various scenarios and models.

# <sup>49</sup> Contents

<sup>50</sup>	<b>Introduction</b>	<b>1</b>
<sup>51</sup>	<b>1 Theoretical Framework of Supersymmetry searches</b>	<b>2</b>
<sup>52</sup>	<b>1.1 The Standard Model</b> . . . . .	2
<sup>53</sup>	<b>1.1.1 Electroweak Symmetry Breaking and the Higgs mechanism</b> . . . . .	6
<sup>54</sup>	<b>1.1.2 Flaws of the Standard Model</b> . . . . .	8
<sup>55</sup>	<b>1.2 Supersymmetry</b> . . . . .	10
<sup>56</sup>	<b>1.2.1 Why SUSY?</b> . . . . .	11
<sup>57</sup>	<b>1.2.2 Minimal Supersymmetric Standard Model</b> . . . . .	12
<sup>58</sup>	<b>1.2.3 Third generation SUSY</b> . . . . .	15
<sup>59</sup>	<b>2 The ATLAS Experiment at the LHC</b>	<b>18</b>
<sup>60</sup>	<b>2.1 The LHC</b> . . . . .	18
<sup>61</sup>	<b>2.2 The ATLAS Detector</b> . . . . .	20
<sup>62</sup>	<b>2.2.1 The Magnet System</b> . . . . .	22
<sup>63</sup>	<b>2.2.2 The Inner Detector</b> . . . . .	23
<sup>64</sup>	<b>2.2.3 The Calorimeters</b> . . . . .	26
<sup>65</sup>	<b>2.2.4 The Muon Spectrometer</b> . . . . .	27
<sup>66</sup>	<b>2.3 The ATLAS Trigger System</b> . . . . .	28
<sup>67</sup>	<b>2.3.1 Level 1 Trigger</b> . . . . .	30
<sup>68</sup>	<b>2.3.2 High-Level Trigger</b> . . . . .	30
<sup>69</sup>	<b>3 The <i>b</i>-jet Trigger Signature in ATLAS</b>	<b>31</b>
<sup>70</sup>	<b>3.1 Trigger Efficiency</b> . . . . .	31
<sup>71</sup>	<b>4 Event Simulation and Reconstruction</b>	<b>32</b>
<sup>72</sup>	<b>4.1 Event Generation</b> . . . . .	32
<sup>73</sup>	<b>4.1.1 Parton Distribution Functions (PDFs)</b> . . . . .	32

74	4.1.2 Matrix Element Calculation . . . . .	32
75	4.1.3 Parton Showers . . . . .	32
76	4.1.4 Hadronisation . . . . .	32
77	4.2 Detector Simulation . . . . .	32
78	<b>5 Stop searches in final states with jets and missing transverse energy</b>	33
79	<b>6 Results and Statistical Intepretations</b>	34
80	<b>Trigger</b>	35
81	<b>Bibliography</b>	36

## <sup>82</sup> List of Tables

<sup>83</sup>	1.1 Forces and mediators described by the SM . . . . .	5
<sup>84</sup>	1.2 Main free parameters introduced by soft supersymmetry breaking in the	
<sup>85</sup>	MSSM. . . . .	13
<sup>86</sup>	1.3 SUSY particles in the MSSM . . . . .	15

# <sup>87</sup> List of Figures

88	1.1	The Higgs potential in the complex plane. . . . .	8
89	1.2	Summary of several Standard Model total production cross section measurements, corrected for leptonic branching fractions, compared to the corresponding theoretical expectations. All theoretical expectations were calculated at NLO or higher. The luminosity used for each measurement is indicated close to the data point. Uncertainties for the theoretical predictions are quoted from the original ATLAS papers. They were not always evaluated using the same prescriptions for PDFs and scales. Not all measurements are statistically significant yet [1]. . . . .	9
90			
91			
92			
93			
94			
95			
96			
97	1.3	The inverse couplings of electromagnetic (dashed blue), weak (dashed red) and strong (solid green) interactions with the SM (left) and a supersymmetric model (right). In the SM the three lines do not meet at one point, but with the introduction of supersymmetry, and assuming that the supersymmetric particles are not heavier than about 1 TeV, they do meet. This is an indication that supersymmetry could be discovered at the LHC. . . . .	12
98			
99			
100			
101			
102			
103	1.4	NLO+NLL production cross sections as a function of mass at $\sqrt{s} = 13\text{TeV}$ [2]	16
104	1.5	Illustration of stop decay modes in the plane stop-neutralino mass plane where the latter is assumed to be the lightest supersymmetric particle and the only one present among the decay products. The dashed blue lines indicate thresholds separating regions where different processes dominate.	17
105			
106			
107			
108	2.1	CERN Accelerator complex. The LHC is the last ring (dark grey line). Smaller machines are used for early-stage acceleration and also to provide beams for other experiments [3]. . . . .	20
109			
110			
111	2.2	Cut-away view of the ATLAS detector. The dimensions of the detector are 25 m in height and 44 m in length. The overall weight of the detector is approximately 7000 tonnes [3]. . . . .	21
112			
113			

114	2.3 The ATLAS magnet system. . . . .	22
115	2.4 The ATLAS Inner Detector . . . . .	24
116	2.5 A computer generated image of the full calorimeter. . . . .	26
117	2.6 Cut-away view of the ATLAS muon system [4]. . . . .	28
118	2.7 The ATLAS TDAQ system. L1Topo and FTK were being commissioned during 2015 and not used for the results shown in this thesis [5]. . . . .	29
119		

# <sup>120</sup> Introduction

<sup>121</sup> Last thing to write

<sup>122</sup> **1** | <sup>123</sup> **Theoretical Framework of Super-**  
<sup>123</sup> **symmetry searches**

<sup>124</sup> *A theory is something nobody believes, except the person who made it. An experiment is something everybody believes, except the person who made it.*

---

Albert Einstein

<sup>125</sup> The Standard Model (SM) of particle physics is an effective theory that aims to provide  
<sup>126</sup> a general description of fundamental particles and the phenomena we see in nature, i. e.  
<sup>127</sup> the way they interact. Unfortunately, our understanding of nature is still limited due to  
<sup>128</sup> some opened question to which the SM is not able to answer to, yet.

<sup>129</sup> In this chapter, an overview of the SM will be presented in Section 1.1 together with  
<sup>130</sup> the limitations of such theory and some of the reasons behind the need of an extension.  
<sup>131</sup> For the last decades theoretical physicsts have been trying to provide extensions to the  
<sup>132</sup> SM, the so-called beyond-the-SM theories. Among these, one of the most popular, Super-  
<sup>133</sup> symmetry which will be discussed in Section 1.2.

<sup>134</sup> **1.1 The Standard Model**

<sup>135</sup> The 20<sup>th</sup> century can be considered a quantum revolution. Several experiments led to  
<sup>136</sup> discoveries which were found to be, together with the formalised theory, a solid base of  
<sup>137</sup> the Standard Model of particle physics and our description of nature. Several particles  
<sup>138</sup> were predicted first by the SM and then experimentally observed e. g. the  $W$  and the  $Z$   
<sup>139</sup> bosons, the  $\tau$  lepton, [6], and more recently the Higgs boson at the LHC discovered by  
<sup>140</sup> ATLAS [7] and CMS [8].

<sup>141</sup> The SM lays on a Quantum Field Theory (QFT) where particles are treated like fields.  
<sup>142</sup> It can describe three of the four fundamental forces; weak, electromagnetic, and strong.  
<sup>143</sup> As of today, gravity is not considered in the SM. Sections 1.1 and 1.1.2 will be focused  
<sup>144</sup> on the description of the fields together with the carriers of the information, and on the  
<sup>145</sup> limitations that such theory implies, respectively.

<sup>146</sup> The most general classification of the particles within the SM can be made by means of  
<sup>147</sup> spin. Fermions have half-integer spin values - and are usually referred to as matter -, and  
<sup>148</sup> bosons have integer-spin values. A noteworthy subset of bosons is formed by the Spin-1  
<sup>149</sup> bosons (also known as gauge bosons). These can be considered the information carriers  
<sup>150</sup> or, in fact, the mediators of the forces.

## <sup>151</sup> Fermions

<sup>152</sup> Six quarks and six leptons belong to the fermions family. In particular, fermions can be  
<sup>153</sup> grouped into three generations. Each generation contains four particles; one up- and one  
<sup>154</sup> down-type quark, one charged lepton and one neutral lepton. The masses of the charged  
<sup>155</sup> leptons and quarks increase with the generation. The six quarks of the SM can be grouped  
<sup>156</sup> into three doublets:

$$\begin{pmatrix} u \\ d \end{pmatrix}, \quad \begin{pmatrix} c \\ s \end{pmatrix}, \quad \begin{pmatrix} t \\ b \end{pmatrix}$$

<sup>157</sup> The up-type quarks (up, charm, top) have charge  $+\frac{2}{3}e$  and the down-type quarks (down,  
<sup>158</sup> strange, beauty/bottom) have charge  $-\frac{1}{3}e$ , where  $e$  is the electron charge. Quarks also  
<sup>159</sup> have another quantum number that can be seen as the analogue of the electric charge,  
<sup>160</sup> which is the colour charge. This can exist in three different states; "red", "green" and  
<sup>161</sup> "blue". Moreover, as a consequence of *confinement*, which will be discussed later on in  
<sup>162</sup> this section, quarks cannot exist as free particles. They rather group to form hadronic  
<sup>163</sup> matter, also known as *hadrons*. There are two kinds of hadrons; mesons and baryons.  
<sup>164</sup> Mesons are quark-antiquark systems, e.g. the pion, and baryons are three-quark system,  
<sup>165</sup> e.g. protons and neutrons. Quarks and anti-quarks have a baryon number of  $\frac{1}{3}$  and  $-\frac{1}{3}$ ,  
<sup>166</sup> respectively.

<sup>167</sup> There are six leptons and they can be classified in charged leptons (electron  $e$ , muon  
<sup>168</sup>  $\mu$ , tau  $\tau$ ) and neutral leptons (electron neutrino  $\nu_e$ , muon neutrino  $\nu_\mu$ , tau neutrino  $\nu_\tau$ ).

$$\begin{pmatrix} \nu_e \\ e^- \end{pmatrix}, \quad \begin{pmatrix} \nu_\mu \\ \mu^- \end{pmatrix}, \quad \begin{pmatrix} \nu_\tau \\ \tau^- \end{pmatrix}$$

<sup>169</sup> Each lepton has a characteristic quantum number, called lepton number ( $L$ ). Negatively  
<sup>170</sup> (positively) charged leptons have  $L = -1$  ( $L = 1$ ) and neutral leptons have  $L = 0$ . The  
<sup>171</sup> lepton number is conserved in all the interactions.

## <sup>172</sup> Forces of Nature

<sup>173</sup> Forces in the SM are described by gauge theories, where the interactions is mediated by  
<sup>174</sup> a vector gauge boson.

<sup>175</sup> The electromagnetic force is described by Quantum ElectroDynamics (QED) and, as  
<sup>176</sup> its mediator is the photon ( $\gamma$ ) which couples to charged particles, it only affects charged  
<sup>177</sup> leptons and quarks, not neutrinos. They are instead affected by the weak force which is  
<sup>178</sup> mediated by the bosons  $W^\pm$  and  $Z^0$ .

<sup>179</sup> The weak interaction is associated with handedness (the projection of a particle spin  
<sup>180</sup> onto its direction of motion). Both leptons and quarks have left- and right-handed com-  
<sup>181</sup> ponents. However, only the left-handed (right-handed) component for neutrinos (anti-  
<sup>182</sup> neutrinos) has been observed. This means that nature prefers to produce left-handed  
<sup>183</sup> neutrinos and right-handed anti-neutrinos, which is the so-called parity violation.

<sup>184</sup> The strong interactions, mediated by the gluon (electrically neutral and massless), is  
<sup>185</sup> described by Quantum ChromoDynamics (QCD). Its coupling increases with increasing  
<sup>186</sup> distance and is smaller at short range. Moreover, due to gluon self interactions, two  
<sup>187</sup> different phenomena arise; *confinement*: neither quarks nor gluons are observed as free  
<sup>188</sup> particles, but only colourless “singlet” states can be observed as “jets”, namely collim-  
<sup>189</sup> ated cone-shaped sprays of hadrons; *asymptotic freedom*: interactions between quarks and  
<sup>190</sup> gluons become weaker as the energy scale increases and the corresponding length scale  
<sup>191</sup> decreases.

<sup>192</sup> Table 1.1 summarises the forces described in the SM and their mediators’ main char-  
<sup>193</sup> acteristics. Finally, the gravitational force, which is believed to be mediated by the grav-  
<sup>194</sup> iton, is not included in Table 1.1 as it is not part of the SM.

## <sup>195</sup> Symmetries and Gauge Groups

<sup>196</sup> In 1915, the mathematician Emmy Noether (23 March 1882 – 14 April 1935) proved that  
<sup>197</sup> every differentiable symmetry of the action - defined as the integral over space of a Lag-

Table 1.1: Forces and mediators described by the SM

Force	Name	Symbol	Mass [GeV]	Charge
Electromagnetic	Photon	$\gamma$	0	0
Weak	W	$W^\pm$	80.398	$\pm e$
	Z	$Z^0$	91.188	0
Strong	Gluon	$g$	0	0

198 rangian density function - of a physical system has a corresponding conservation law.  
199 More generally, a symmetry is a property of a physical system. Under certain transforma-  
200 tions this property is preserved.

201 A gauge theory in QFT, is a theory in which the Lagrangian is invariant under a con-  
202 tinuous group of local transformation. Group theory was then adopted to describe the  
203 symmetries conserved in the SM. The gauge group of the theory is the *Lie Group*. It con-  
204 tains all the transformations between possible gauges. The Lie algebra of group generators  
205 is therefore associated with any Lie group and for each group generator there emerges a  
206 corresponding field: the gauge field. The quanta of the gauge fields are called *gauge bo-*  
207 *sons*.

208 The three SM interactions can therefore be mathematically described by the following:

$$U(1)_Y \otimes SU(2)_L \otimes SU(3)_C \quad (1.1)$$

209 Here,  $Y$  is the weak hypercharge, used to estimate the correlation between the electric  
210 charge ( $Q$ ) and the third component of the weak isospin ( $I_3$ ) via the relation  $Q = I_3 + Y/2$ ,  
211 where  $I_3$  can either be  $\pm 1/2$  or 0 for left-handed and right-handed particles, respectively;  
212  $C$  the colour charge and  $L$  the left-handedness.

213 As of today, we can describe three of the four forces of nature with group theory. QED  
214 is an Abelian gauge theory with  $U(1)$  as symmetry group, with the electromagnetic four-  
215 potential as its gauge field and with the photon as its gauge boson [9]. The interactions  
216 between charged fermions occurs by the exchange of a massless photon.

217 The weak interaction and the strong interactions are non-Abelian gauge theories with  
218 gauge groups  $SU(2)$  and  $SU(3)$ , respectively. As a consequence of being non-Abelian  
219 the generators commutators are non-vanishing and therefore the gauge bosons can self-  
220 interact. The  $SU(2)$  generators of the weak interaction are the massless gauge bosons  
221  $W_\mu^{\alpha=1,\dots,3}$  and, as mentioned earlier on in this chapter, they violate the parity by acting  
222 only on left-handed particles.

<sup>223</sup> The gauge bosons of  $SU(3)_C$  are eight massless gluons,  $G_\mu^{\alpha=1,\dots,8}$ . The strong interaction  
<sup>224</sup> does not distinguish left- and right-handed particles. Finally, the Quarks that interact  
<sup>225</sup> through weak interaction are mixtures of SM eigenstates as described by the CKM matrix  
<sup>226</sup> [10].

### <sup>227</sup> 1.1.1 Electroweak Symmetry Breaking and the Higgs mechanism

<sup>228</sup> In 1979 Sheldon Glashow, Abdus Salam, and Steven Weinberg were awarded the Nobel  
<sup>229</sup> Prize in Physics for their contributions to the so-called electroweak unification. In  
<sup>230</sup> the mathematical description of the SM in 1.1 the electroweak interaction is described by  
<sup>231</sup>  $U(1)_Y \otimes SU(2)_L$ . The electroweak physical bosons  $W$ ,  $Z$  and  $\gamma$  are related to the four  
<sup>232</sup> unphysical gauge bosons  $W_\mu^{\alpha=1,\dots,3}$  and  $B_\mu^0$ . In particular, to obtain the physical bosons  
<sup>233</sup> the gauge bosons have to mix as follows:

$$\begin{pmatrix} A_\mu \\ Z_\mu \end{pmatrix} = \begin{pmatrix} \cos \theta_W & \sin \theta_W \\ -\sin \theta_W & \cos \theta_W \end{pmatrix} \begin{pmatrix} B_\mu \\ W_\mu^3 \end{pmatrix} \quad (1.2)$$

<sup>234</sup> Here,  $\theta_W$  is the so-called *Weinberg angle* which is the angle by which spontaneous sym-  
<sup>235</sup> metry breaking rotates the original  $W_\mu^3$  and  $B_\mu$ , producing the physical  $Z$ , and the photon.  
<sup>236</sup>  $\theta_W$  can be experimentally determined in terms of the coupling strengths of the  $B_\mu(g_1)$  and  
<sup>237</sup> the  $W_\mu^\alpha(g_2)$  to the fermions using the relation  $\tan \theta_W = g_1/g_2$ . The field mixing of gauge  
<sup>238</sup> bosons that gives birth to the physical ones can be mathematically expressed by the fol-  
<sup>239</sup> lowing:

$$A_\mu = W_\mu^3 \sin \theta_W + B_\mu \cos \theta_W \quad (1.3)$$

<sup>240</sup>

$$Z_\mu = W_\mu^3 \cos \theta_W - B_\mu \sin \theta_W \quad (1.4)$$

<sup>241</sup> where  $A_\mu$  and  $Z_\mu$  represent the photon and the  $Z$  boson, respectively. The charged vector  
<sup>242</sup> bosons,  $W_\mu^\mp$ , and its complex conjugate are defined as:

$$W_\mu^\pm = \frac{1}{\sqrt{2}} (W_\mu^1 \mp iW_\mu^2) \quad (1.5)$$

<sup>243</sup> Mass terms for both gauge bosons and fermionic fields are not invariant under gauge  
<sup>244</sup> transformations and are therefore forbidden by the electroweak gauge. Nonetheless, it is  
<sup>245</sup> proven by experiments that  $W$  and  $Z$  are massive [9], therefore the SM assumption only  
<sup>246</sup> holds if the electroweak symmetry is broken.

<sup>247</sup> The SM Lagrangian can be written as the sum of the various Lagrangians describing  
<sup>248</sup> the three interactions and the masses of the elementary particles as follows:

$$\mathcal{L}_{\text{SM}} = \mathcal{L}_{\text{EWK}} + \mathcal{L}_{\text{QCD}} + \mathcal{L}_{\text{Mass}} \quad (1.6)$$

<sup>249</sup> In order for the SM Lagrangian to remain a renormalisable theory, mass terms ( $\mathcal{L}_{\text{Mass}}$ )  
<sup>250</sup> cannot be inserted by hand. A mechanism, that can preserve the gauge symmetry in  
<sup>251</sup> the SM and, that can solve the inconsistency arisen from the mass difference between  
<sup>252</sup> the gauge bosons and the physical ones, is needed. A British theoretical physicist, Peter  
<sup>253</sup> Higgs (29 May 1929, Newcastle upon Tyne, UK), came up with a brilliant solution for  
<sup>254</sup> which he was awarded the 2013 Physics Nobel Prize. In the 1960s, Higgs proposed that  
<sup>255</sup> broken symmetry in electroweak theory could explain the origin of masses of elementary  
<sup>256</sup> particles, and in particular of  $W$  and  $Z$  bosons: the Higgs mechanism was given birth.  
<sup>257</sup> The mechanism introduces a scalar field, known as the Higgs field, thought to couple to  
<sup>258</sup> both massive fermions and bosons.

<sup>259</sup> In the SM the Higgs field is a doublet in  $SU(2)$ :

$$\phi = \begin{pmatrix} \phi^+ \\ \phi^0 \end{pmatrix} \quad (1.7)$$

<sup>260</sup> with  $\phi^+$  and  $\phi^0$  being generic complex fields:

$$\phi^+ = \frac{\phi_1 + i\phi_2}{\sqrt{2}}, \quad \phi^0 = \frac{\phi_3 + i\phi_4}{\sqrt{2}} \quad (1.8)$$

<sup>261</sup> Consider a Lagrangian of the form:

$$\mathcal{L}_{\text{Higgs}} = (\partial_\mu \phi)^* (\partial^\mu \phi) - V(\phi) \quad (1.9)$$

<sup>262</sup> Renormalizability and  $SU(2)_L \otimes U(1)_Y$  invariance require the Higgs potential to be of the  
<sup>263</sup> following form:

$$V(\phi) = \mu^2 \phi^\dagger \phi + \lambda (\phi^\dagger \phi)^2 \quad (1.10)$$

<sup>264</sup> Eq. 1.9 is the Higgs Lagrangian if  $\phi$  is chosen to be the following:

$$\phi = \begin{pmatrix} \phi^+ \\ \phi^0 \end{pmatrix} = \begin{pmatrix} G^+ \\ \frac{1}{\sqrt{2}}(v + H + iG^0) \end{pmatrix}$$

265 Here, the complex scalar field  $G^\pm$  and the real scalar field  $G^0$  correspond to Goldstone  
 266 bosons, and the real scalar field  $H$  is the SM Higgs boson field [11]. These massless scalars  
 267 are absorbed due to the gauge transformations by the electroweak gauge bosons of the SM:

$$\phi = \begin{pmatrix} \phi^+ \\ \phi^0 \end{pmatrix} = \begin{pmatrix} 0 \\ \frac{1}{\sqrt{2}}(v + H) \end{pmatrix} \quad (1.11)$$

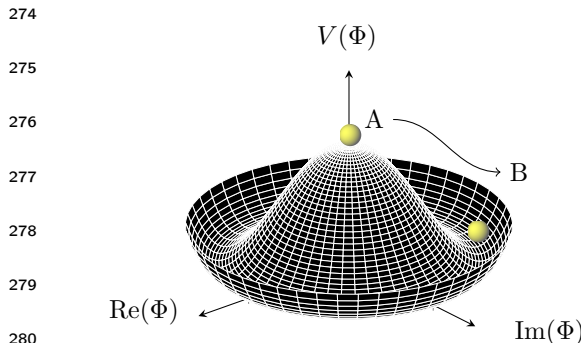
268 The Higgs potential in Eq. 1.10 is displayed in Fig. 1.1 if  $\lambda$  and  $\mu$  are chosen to be  
 269 real. Such potential has a non-zero ground state,  $v$ , also known as *vacuum expectation*  
 270 *value* (VEV):

$$\phi_0 = \begin{pmatrix} 0 \\ \frac{1}{\sqrt{2}}v \end{pmatrix} \quad (1.12)$$

271 Such representation remains invariant under  $U(1)$  allowing electric charge conservation.  
 272 However, the SM gauge symmetry 1.1 is broken into  $SU(2)_L \otimes U(1)_Y$ .

273

In summary, to generate particle masses  
 gauge symmetry must be broken. However,  
 in order for the theory to remain  
 renormalisable, the global Lagrangian  
 symmetry must be preserved. This can be  
 solved introducing the concept of *spontane-*  
*ous* symmetry breaking (SSB): a mechani-  
 sm that allows a symmetric Lagrangian,  
 but not a symmetric VEV. In particular,



282 Figure 1.1: The Higgs potential in the complex plane.

283  
 284 of states, that transform under  $T_X$  as the elements of a multiplet, the symmetry is spon-  
 285 taneously broken if one of those states is arbitrarily chosen as the ground state of the sys-  
 286 tem. The interaction of the Higgs field with the  $SU(2) \otimes U(1)$  gauge fields,  $W_\mu^\alpha = 1, 2, 3$ ,  
 287 result in the three gauge bosons fields acquiring mass whilst the  $B_0$  field stays massless.

### 288 1.1.2 Flaws of the Standard Model

289 During Run 1 and 2 of the LHC, the SM has been extensively validated, as shown in Fig.  
 290 1.2: the agreement, between the measured production cross section of various SM pro-  
 291 cesses and the SM predictions, looks very good. However, the reasons behind the mass

difference between the three generations of fermions are still not explained by the SM because masses are treated as free parameters of the theory. In addition, there are some fundamental questions that have still no answer and they will be briefly discussed this section.

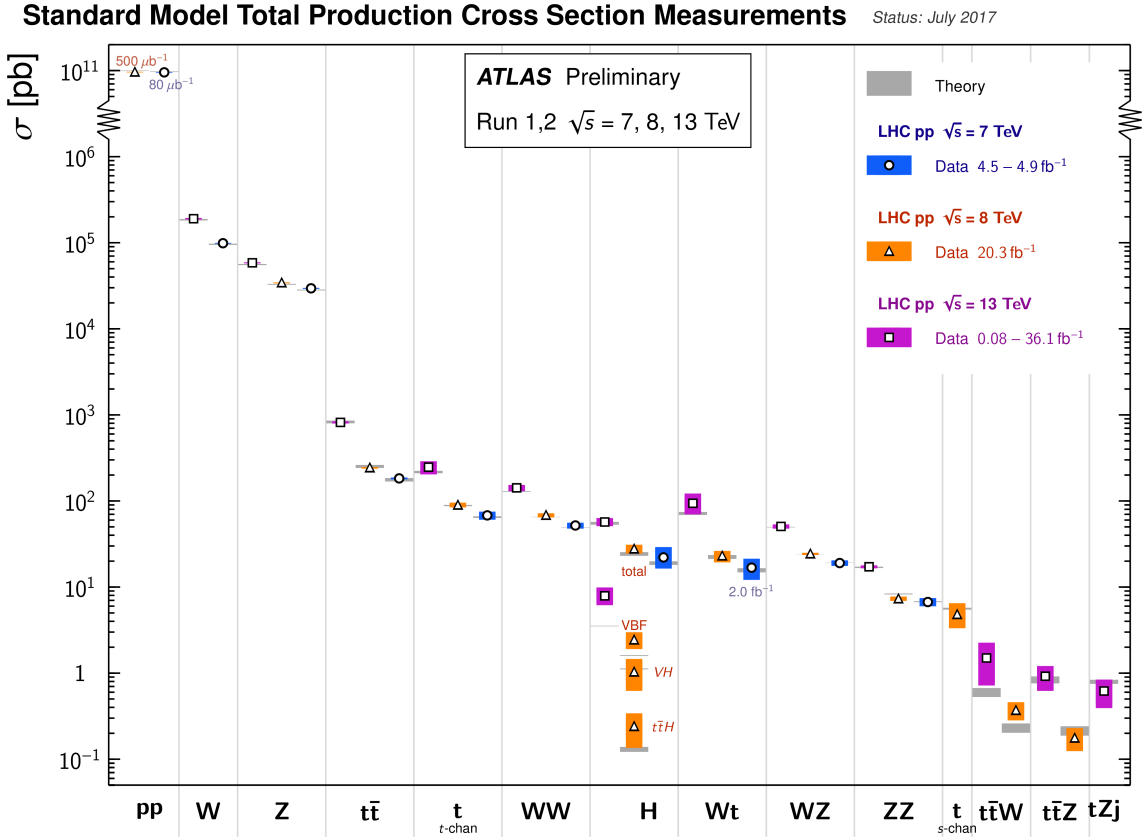


Figure 1.2: Summary of several Standard Model total production cross section measurements, corrected for leptonic branching fractions, compared to the corresponding theoretical expectations. All theoretical expectations were calculated at NLO or higher. The luminosity used for each measurement is indicated close to the data point. Uncertainties for the theoretical predictions are quoted from the original ATLAS papers. They were not always evaluated using the same prescriptions for PDFs and scales. Not all measurements are statistically significant yet [1].

## 296    Hierarchy Problem

297    Due to the coupling of the Higgs field to the fermionic fields the one-loop corrections to  
 298    the Higgs mass receive several contributions. In particular:

$$\Delta m_H^2 = -\frac{|\lambda_f|^2}{8\pi^2} \Lambda_{\text{UV}}^2 + \dots \quad (1.13)$$

299    here,  $\lambda_f$  is the coupling constant to the fermionic field;  $\Delta m_H^2$  is the difference between  
 300    the observed Higgs mass  $m_H^2$  and the bare mass,  $m_H^0$  (Lagrangian parameter);  $\Lambda_{\text{UV}}$  is

301 the ultraviolet momentum cut-off, selected to be at the Planck scale ( $\sim 2 \cdot 10^{18}$  GeV), at  
302 which a QFT description of gravity is believed to become possible. The correction to the  
303 Higgs mass then, will be around 30 orders of magnitude larger than Higgs mass itself,  
304 in opposition to what has been measured. This difference just mentioned, between the  
305 electroweak scale and the Planck scale arisen from the quantum corrections to the Higgs  
306 mass, is the so-called Hierarchy Problem [12].

### 307 Neutrino Masses

308 The Super-Kamiokande Collaboration first, in 1998 [13], and SNO Collaboration later, in  
309 2001 [14], have provided measurements of the neutrino flux from solar and atmospheric  
310 sources. The Nobel Prize in Physics 2015 was awarded jointly to Takaaki Kajita and Arthur  
311 B. McDonald “for the discovery of neutrino oscillations, which shows that neutrinos have  
312 mass” [15]. Such feature contradicts the absence of a mechanism for mass generation for  
313 the neutrinos.

314 Various exotic solutions are on the market: one possible solution could be to add the  
315 so-called Majorana mass terms for the neutrino (seesaw mechanism). Neutrino physics  
316 could unveil physics beyond the SM.

### 317 Dark Matter

318 Although dark matter (DM) has never been directly observed, its existence is inferred  
319 from its gravitational effects. For example, looking at galaxies rotation, it was observed  
320 that the rotation speed was higher than expected, given the amount of visible matter. Two  
321 different reasoning arose during the last century to justify such effect either there is matter  
322 that cannot be seen by us (in terms of visible light), which contributes to the galactic mass;  
323 or the general relativity works differently at galactic distances. The former is believed to  
324 be the most likely and it implies the existence of new particles which do not interact via  
325 electromagnetic interaction, the so-called Weakly Interacting Massive Particles (WIMPs).

## 326 1.2 Supersymmetry

327 Supersymmetry links gravity with the other fundamental forces of nature by introducing  
328 a space-time symmetry that relates bosons to fermions and vice-versa, via a transforma-  
329 tion of the form of:

$$Q |\text{fermion}\rangle = |\text{boson}\rangle , \quad Q |\text{boson}\rangle = |\text{fermion}\rangle \quad (1.14)$$

<sup>330</sup> For each SM particle there exists a superpartner with a spin difference of  $\Delta s = 1/2$ . As of  
<sup>331</sup> today, superpartners, generally called *sparticles* (where the *s* stands for “scalar”), have not  
<sup>332</sup> been observed yet, resulting in the assumption that SUSY must be a broken symmetry,  
<sup>333</sup> otherwise superpartners would have the same quantum numbers and masses as their  
<sup>334</sup> SM equivalent. However, if sparticles were to be too heavy (close to the Planck scale),  
<sup>335</sup> the hierarchy problem would still remain unsolved. The *soft* SUSY breaking mechanism  
<sup>336</sup> overcomes this problem imposing contrains on the masses of sparticles to a range that can  
<sup>337</sup> be experimentally explored.

<sup>338</sup> In this section an overview of Supersymmetry (SUSY) will be presented, together with  
<sup>339</sup> the motivations behind the success of such theory. Finally, third generation SUSY will be  
<sup>340</sup> discussed as it is the most relevant theoretical support to the analyses presented in this  
<sup>341</sup> work.

### <sup>342</sup> 1.2.1 Why SUSY?

<sup>343</sup> One of the main motivations for SUSY is the cancellation of quadratic divergences to  
<sup>344</sup>  $\Delta m_H^2$ . The introduction of SUSY particles with a half-integer spin difference with re-  
<sup>345</sup> spect to their SM provides a solution to the hierarchy problem. The Higgs mass squared  
<sup>346</sup> potential receives corrections from a new scalar of mass  $m_S$  of the form:

$$\Delta m_H^2 = -\frac{|\lambda_S|^2}{16\pi^2} \left[ \Lambda_{UV}^2 - 2m_S^2 \ln(\Lambda_{UV}/m_S) + \dots \right] \quad (1.15)$$

<sup>347</sup> where,  $\lambda_S$  is the coupling of SUSY particles to the Higgs field. This term cancels the  
<sup>348</sup> fermionic contributions in Eq. 1.13 since the couplings are the same. The experimental  
<sup>349</sup> value of Higgs mass will then not need any fine tuning.

<sup>350</sup> Fig. 1.3 shows the inverse couplings as a function of the scale for both SM and the  
<sup>351</sup> Minimal Supersymmetric Standard Model (MSSM), which will be soon discussed. In the  
<sup>352</sup> SM the three lines, representing electromagnetic (dashed blue), weak (dashed red) and  
<sup>353</sup> strong (solid green) interactions respectively, do not meet at one point, but with the in-  
<sup>354</sup> troduction of supersymmetry, and assuming that the supersymmetric particles are not  
<sup>355</sup> heavier than about 1 TeV, they do meet. This is an indication that supersymmetry could  
<sup>356</sup> be discovered at the LHC. The possible unification of the coupling constants at the Planck  
<sup>357</sup> scale is therefore another good motivation for SUSY searches.

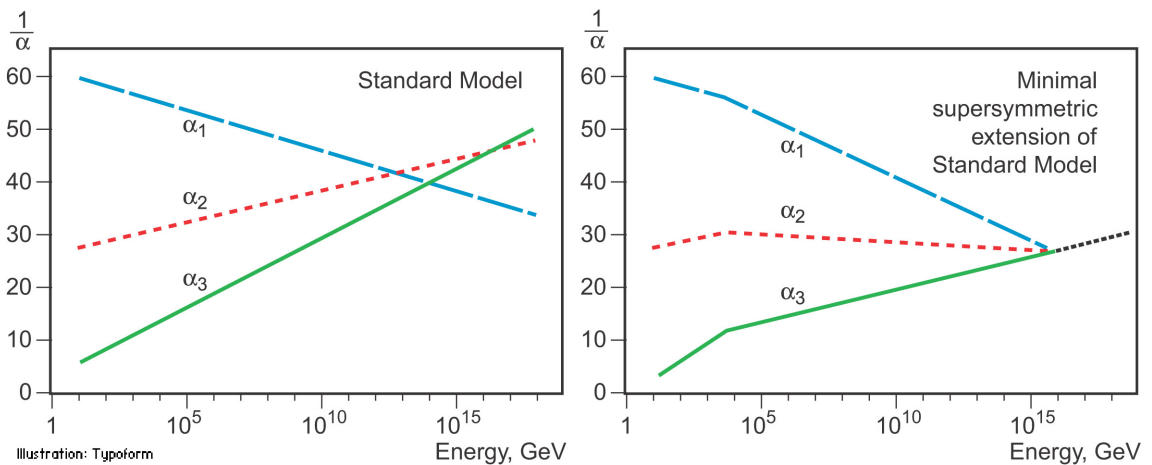


Figure 1.3: The inverse couplings of electromagnetic (dashed blue), weak (dashed red) and strong (solid green) interactions with the SM (left) and a supersymmetric model (right). In the SM the three lines do not meet at one point, but with the introduction of supersymmetry, and assuming that the supersymmetric particles are not heavier than about 1 TeV, they do meet. This is an indication that supersymmetry could be discovered at the LHC.

### 358 1.2.2 Minimal Supersymmetric Standard Model

359 There does not exist a unique extension of a supersymmetric Standard Model, i.e. SUSY  
360 is not a well-defined model but it is more a framework within which various SM exten-  
361 sions can be derived. The Minimal Supersymmetric Standard Model (MSSM), a minimal  
362 supersymmetric extension of the SM [16], is defined by essentially doubling up the num-  
363 ber of particles in the SM theory in order to include all the SM particles as well as their  
364 corresponding superpartners.

### 365 Soft SUSY breaking

366 The mass spectrum of the SUSY particles must sit somewhere at a larger scale than the SM  
367 one, as supersymmetric particles have not been discovered at the mass scale of their SM  
368 partners. This gives us a hint that supersymmetry cannot be an exact symmetry, there has  
369 to be an analogous to the electroweak symmetry breaking discussed in 1.1.1 that breaks  
370 SUSY. In particular, this must be soft or spontaneous such that broken supersymmetry still  
371 provides a solution to the hierarchy problem. This means that some new higher energy  
372 scale particles and interactions have to be added to the MSSM, but it also means that  
373 terms, containing only masses and couplings with positive mass dimension, being gauge  
374 invariant and violating SUSY, have to be added to the Lagrangian which will then be

<sup>375</sup> defined as;

$$\mathcal{L} = \mathcal{L}_{\text{SUSY}} + \mathcal{L}_{\text{soft}} \quad (1.16)$$

<sup>376</sup> Here,  $\mathcal{L}_{\text{SUSY}}$  contains the original SUSY invariant interaction and  $\mathcal{L}_{\text{soft}}$  contains all the  
<sup>377</sup> additional terms. A set of around 100 parameters - depending on the method - are then  
<sup>378</sup> introduced into the theory, and these are catalogued in Table 1.2.

Table 1.2: Main free parameters introduced by soft supersymmetry breaking in the MSSM.

Parameters	Physical Explanation
$M_1, M_2, M_3$	Bino, Wino and gluino masses
$m_{\tilde{Q}_L}$ $m_{\tilde{u}_R}, m_{\tilde{d}_R}$ $m_{\tilde{l}_L}, m_{\tilde{l}_R}$	left-handed squarks masses up- and down-type right-handed squarks masses left- and right-handed sleptons masses
$m_{\tilde{H}_u^2}, m_{\tilde{H}_d^2}$ $ \mu , B$	Up- and down-type higgsino mass squared higgsino mass and the bilinear higgs term
$A_u, A_d, A_e$	Up- and down-type squark sfermion and Higgs interaction trilinear couplings
$\tan \beta$	Ratio of the VEVs of the two higgs doublet fields

### <sup>379</sup> MSSM mass spectrum

<sup>380</sup> As for gauge bosons and the Higgs, there exists MSSM fermionic superpartner. These are  
<sup>381</sup> referred to as *Gauginos* and *Higgsinos* and, differently from the SM, in the MSSM there are  
<sup>382</sup> two complex Higgs doublets:

$$H_u = (H_u^+, H_u^0) \quad H_d = (H_d^0, H_d^-)$$

<sup>383</sup> with their respective VEVs,  $v_d, v_u$  which are constrained by the SM Higgs VEV:

$$v = \sqrt{v_u^2 + v_d^2}$$

<sup>384</sup> As per SM gauge bosons, the gaugino masses are affected by electroweak symmetry  
<sup>385</sup> breaking. The new mass terms, introduced in the  $\mathcal{L}_{\text{soft}}$ , mix to form the mass eigenstates  
<sup>386</sup> of the sparticles. Nautral Winos,  $\tilde{W}^0$ , Binos,  $\tilde{B}^0$  and higgsinos  $\tilde{H}^0$  mix to form the four

<sup>387</sup> neutralinos  $\tilde{\chi}_i^0$  ( $i = 1, 2, 3, 4$ ) as it follows;

$$\begin{pmatrix} \tilde{\chi}_1^0 \\ \tilde{\chi}_2^0 \\ \tilde{\chi}_3^0 \\ \tilde{\chi}_4^0 \end{pmatrix} = \begin{pmatrix} M_1 & 0 & -c_\beta s_W m_Z & c_W s_\beta m_Z \\ 0 & M_2 & c_\beta c_W m_Z & -c_W s_\beta m_Z \\ -c_\beta s_W m_Z & c_\beta s_W m_Z & 0 & -\mu \\ s_\beta c_W m_Z & -s_\beta c_W m_Z & -\mu & 0 \end{pmatrix} \begin{pmatrix} \tilde{B}^0 \\ \tilde{W}^0 \\ \tilde{H}_u^0 \\ \tilde{H}_d^0 \end{pmatrix} \quad (1.17)$$

<sup>388</sup> Here,  $c_\beta = \cos \beta$ ,  $(s_\beta) = \sin \beta$ ,  $c_W = \cos \theta_W$  and  $(s_W) = \sin \theta_W$ .  $M_1$ ,  $M_2$  are related to gaugino masses and  $\mu$  to higgsino mass,  $\beta$  is the ratio of the electroweak coupling constants and  $\theta_W$  is the ratio of the VEVs of the two Higgs doublet fields, and finally,  $m_Z$  ( $m_W$ ) is the mass of the  $Z$  ( $W$ ) boson. The neutralino indeces are conventionally assumed to increase with their masses.

<sup>393</sup> The charged winos  $\tilde{W}^\pm$  and higgsinos  $\tilde{H}^\pm$  mix to form four *charginos*,  $\tilde{\chi}_i^\pm$  ( $i = 1, 2$ ) as it follows;

$$\begin{pmatrix} \tilde{\chi}_1^\pm \\ \tilde{\chi}_2^\pm \end{pmatrix} = \begin{pmatrix} M_2 & \sqrt{2}m_W \sin \beta \\ \sqrt{2}m_W \cos \beta & \mu \end{pmatrix} \begin{pmatrix} \tilde{W}^\pm \\ \tilde{H}^\pm \end{pmatrix} \quad (1.18)$$

<sup>395</sup> Charginos and neutralinos, given birth by the mixing described in Eq. 1.18 and 1.17, will be referred to as bino-like, wino-like or higgsino-like depending on their phenomenology. Gluinos do not mix as they carry colour charge, and its mass is linked to  $M_3$ .

<sup>398</sup> Sleptons and squarks states also mix due to electroweak symmetry breaking, although <sup>399</sup> it is assumed to be zero except for the third generation particles. Stop,  $\tilde{t}_L$ ,  $\tilde{t}_R$ , sbottom  $\tilde{b}_L$ , <sup>400</sup>  $\tilde{b}_R$ , and stau,  $\tilde{\tau}_L$ ,  $\tilde{\tau}_R$  mix to give mass eigenstates,  $\tilde{t}_1$ ,  $\tilde{t}_2$ ,  $\tilde{b}_1$ ,  $\tilde{b}_2$ ,  $\tilde{\tau}_1$ ,  $\tilde{\tau}_2$ , respectively. As with <sup>401</sup> the neutralinos and charginos, the convention is to refer to the one with the lower index as <sup>402</sup> the lighter one. Finally, the Higgs sector is also affected. There are five mass eigenstates, <sup>403</sup>  $h^0$ ,  $H^0$ ,  $A^0$ , and  $H^\pm$ . These, together with the other MSSM particles are listed in Table 1.3.

#### <sup>404</sup> R-parity

<sup>405</sup> The most general MSSM can contain operators that violate baryon and / or lepton number, <sup>406</sup> thus allowing proton decays. The non-observation of proton decays forbids the existence <sup>407</sup> of such terms. A possibility to avoid these operators is to introduce a new discrete symmetry named R-parity. The conserved quantum number is defined as:

$$P_R = (-1)^{3(B-L)+2s} \quad (1.19)$$

<sup>409</sup> where  $B$ ,  $L$  and  $s$  are the baryon, lepton, and spin number, respectively.

Table 1.3: SUSY particles in the MSSM

Name	Spin	Gauge Eigenstates	Mass Eigenstates
Squarks ( $\tilde{q}$ )	0	$\tilde{u}_L \tilde{u}_R \tilde{d}_L \tilde{d}_R$	(same)
		$\tilde{c}_L \tilde{c}_R \tilde{s}_L \tilde{s}_R$	(same)
		$\tilde{t}_L \tilde{t}_R \tilde{b}_L \tilde{b}_R$	$\tilde{t}_1 \tilde{t}_2 \tilde{b}_1 \tilde{b}_2$
Sleptons ( $\tilde{l}$ )	0	$\tilde{e}_L \tilde{e}_R \tilde{\nu}_L$	(same)
		$\tilde{\mu}_L \tilde{\mu}_R \tilde{\nu}_L$	(same)
		$\tilde{\tau}_L \tilde{\tau}_R \tilde{\nu}_{\tau}$	$\tilde{\tau}_1 \tilde{\tau}_2 \tilde{\nu}_{\tau}$
Higgs bosons	0	$H_u^0 H_d^0 H_u^+ H_d^-$	$h^0 H^0 A^0 H^{\pm}$
Neutralinos ( $\tilde{\chi}_j^0$ )	1/2	$\tilde{B}^0 \tilde{W}^0 \tilde{H}_u^0 \tilde{H}_d^0$	$\tilde{\chi}_1^0 \tilde{\chi}_2^0 \tilde{\chi}_3^0 \tilde{\chi}_4^0$
Charginos ( $\tilde{\chi}_i^{\pm}$ )	1/2	$\tilde{W}^{\pm} \tilde{H}_u^{\pm} \tilde{H}_d^{\mp}$	$\tilde{\chi}_1^{\pm} \tilde{\chi}_2^{\pm}$
Gluino	1/2	$\tilde{g}$	(same)
Gravitino	3/2	$\tilde{G}$	(same)

If a certain SUSY model is  $R$ -parity conserving, then the SM particles have  $R = 1$  and SUSY partners have  $R = -1$ . When  $R$ -parity conservation is imposed on MSSM models, the mixing between particles and sparticles cannot occur, resulting in the number of SUSY particles to be even at every interaction vertex. Furthermore, all sparticles must be pair-produced and the Lightest Supersymmetric Particle (LSP) has to be stable and can therefore be a good Dark Matter candidate. Heavier sparticles can only decay to odd numbers of it.

In this work only  $R$ -parity conserving (RPC) models, where the  $\tilde{\chi}_1^0$  is assumed to be the LSP, were considered.

### 1.2.3 Third generation SUSY

As mentioned earlier on in this chapter, the introduction of SUSY particles overcomes the problem of an unnatural fine-tuning to the Higgs mass due to its quadratic corrections, given that the stops have masses typically around 1 TeV.

Stop pair production analyses are very challenging due to the cross section being around a factor of six smaller than  $t\bar{t}$  production (when  $m_{\tilde{t}_1} \sim m_t$ ). Furthermore, the cross-section of such processes dramatically decreases with increasing  $m_{\tilde{t}_1}$ . Nonetheless, searches for direct  $\tilde{t}_1$  production with  $\tilde{t}_1 \rightarrow t + \tilde{\chi}_1^0$  are sensitive in a scenario where  $m_{\tilde{t}_1} \gg m_t + m_{\tilde{\chi}_1^0}$  as the large  $E_T^{\text{miss}}$ , from the neutralinos, provides discriminating power for  $t\bar{t}$  rejection.

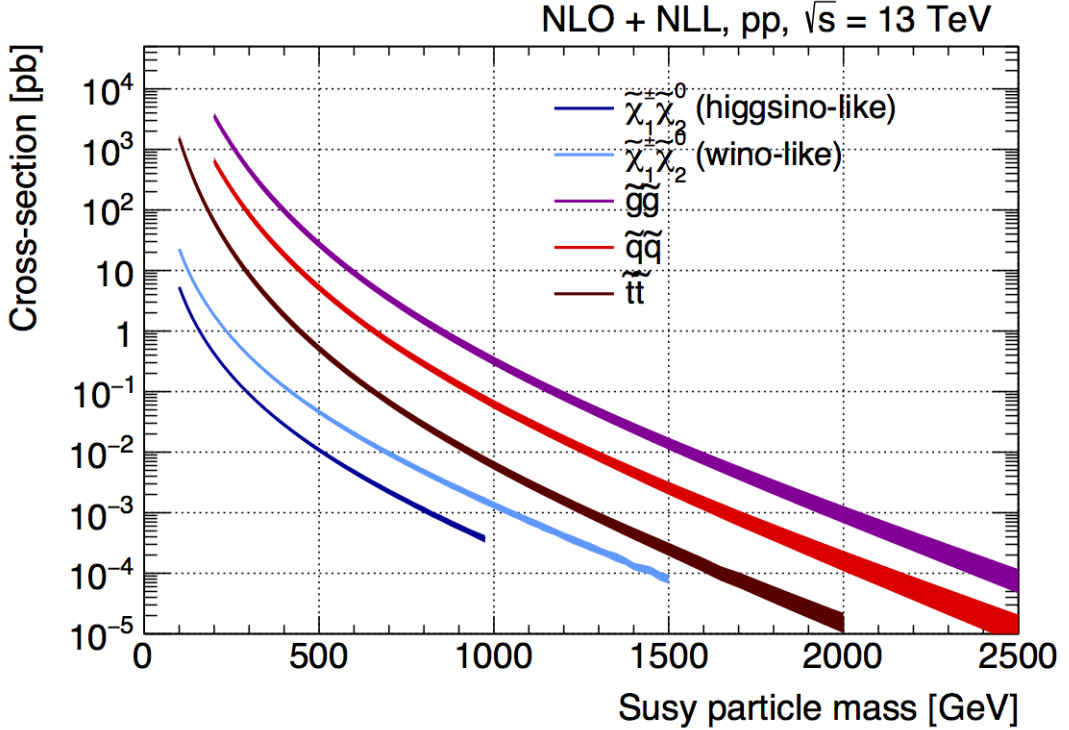


Figure 1.4: NLO+NLL production cross sections as a function of mass at  $\sqrt{s} = 13 \text{ TeV}$  [2]

Fig. 1.4 shows SUSY particles production cross-sections for squarks that do not contribute to gluino production diagrams and vice versa, i.e. treating squarks and gluinos as *decoupled* making the cross section of squark pair-production be the same for all families. While gluinos production cross-sections are fairly large, SUSY electroweak production cross-sections of neutralinos and charginos are considerably lower. Sleptons production cross-section, which is not displayed, would sit just below higgsino-like chargino/neutralino production cross-section.

The large number of particles and degrees of freedom in the MSSM brings in some parametrisation issues that lead to a non-trivial theoretical interpretation of the results of a certain analysis. However, simplified models represent a good workaround. The strategy [17] practically is to focus the attention only on a specific signal process without caring about other contributions. The analysis will then be optimised to address that particular signal, e.g. direct stop pair-production in the two-body channel  $t \rightarrow \tilde{t}_1 + \tilde{\chi}_1^0$  without including the remaining SUSY mass spectrum. Such simplified models allow a theoretical reinterpretation of the results and provide a powerful tool to constrain various models. In this work only analyses laying their theoretical assumptions on such simplified models will be presented.

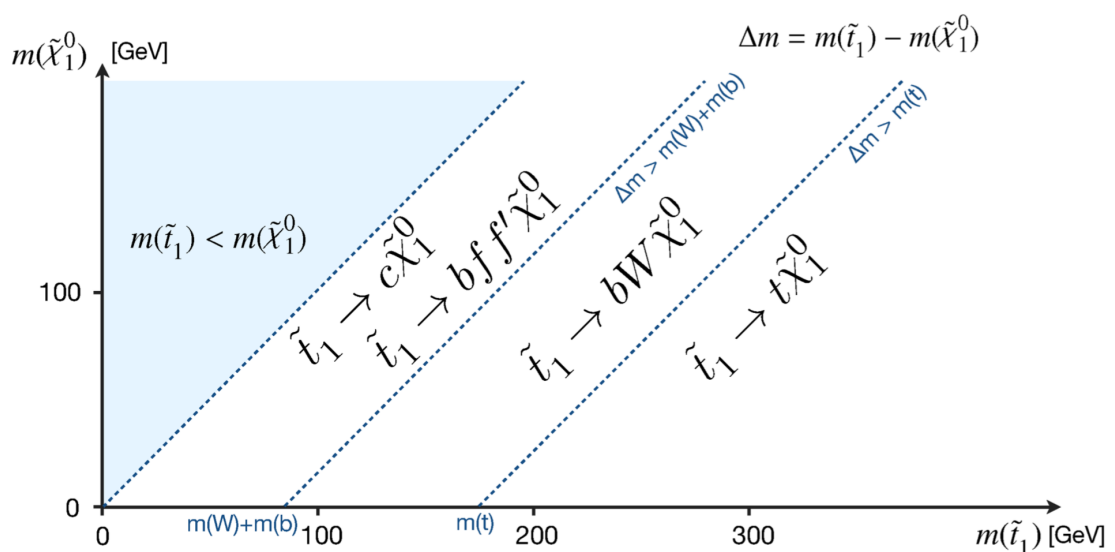


Figure 1.5: Illustration of stop decay modes in the plane stop-neutralino mass plane where the latter is assumed to be the lightest supersymmetric particle and the only one present among the decay products. The dashed blue lines indicate thresholds separating regions where different processes dominate.

## **2 | The ATLAS Experiment at the LHC**

446   ATLAS (A Toroidal LHC ApparatuS) is one of the four main experiments (ATLAS, CMS,  
 447   ALICE, LHCb) taking data at a center-of-mass energy of 13 TeV using beams delivered by  
 450   the Large Hadron Collider (LHC). In this chapter an overview of the LHC will be given  
 451   in Section 2.1, then the ATLAS detector will be described in Section 2.2, and finally the  
 452   Trigger system, used to cleverly store the data, will be described in Section 2.3. A more  
 453   in-depth description of the Trigger algorithms I have been involved in will be given in  
 454   Chapter 3.

### **455   2.1 The LHC**

456   As of today, the LHC is the world's largest and most powerful particle accelerator. It was  
 457   designed to help answer some of the fundamental open questions in particle physics by  
 458   colliding protons at an unprecedented energy and luminosity. It is located at the European  
 459   Organisation for Nuclear Research (CERN), in the Geneva area, at a depth ranging from  
 460   50 to 175 metres underground. It consists of a 27-kilometre ring made of superconducting  
 461   magnets, and inside it two high-energy particle beams travel in opposite directions and  
 462   in separate beam pipes.

463       The beams are guided around the ring by a strong magnetic field generated by coils -  
 464   made of special electric cables - that can operate in a superconducting regime. 1232 super-  
 465   conducting dipole and 392 quadrupole magnets, with an average magnetic field of 8.3 T,  
 466   are employed and kept at a temperature below 1.7 K, in order to preserve their supercon-  
 467   ducting properties. The formers are used to bend the beams and the latters to keep them  
 468   focused while they get accelerated.

469       The collider first went live on September 2008 even though, due to a magnet quench  
 470   incident that damaged over 50 superconducting magnets, it has been operational since

<sup>471</sup> November 2009 when low-energy beams circulated in the tunnel for the first time since the  
<sup>472</sup> incident. This also marked the start of the main research programme and the beginning  
<sup>473</sup> of the so-called Run 1: first operational run (2009 - 2013).

#### <sup>474</sup> Performance of the LHC

<sup>475</sup> In June 2015 the LHC restarted delivering physics data, after a two-year break, the so-  
<sup>476</sup> called Long Shutdown 1 (LS1), during which the magnets were upgraded to handle the  
<sup>477</sup> current required to circulate 7-TeV beams. It was the beginning of the so-called Run 2 -  
<sup>478</sup> second operational run (2015-2018) - during which LHC has collided up to  $10^{11}$  bunches  
<sup>479</sup> of protons every 25 ns at the design luminosity - the highest luminosity the detector was  
<sup>480</sup> designed to cope with - of  $2 \cdot 10^{34} \text{ cm}^{-2} \text{s}^{-1}$ . The definition of the luminosity is:

$$\mathcal{L} = f \frac{n_b N_1 N_2}{4\pi\sigma_x\sigma_y} \quad (2.1)$$

<sup>481</sup> where  $N_1$  and  $N_2$  are the number of protons per bunch in each of the colliding beams,  $f$   
<sup>482</sup> is the revolution frequency of the bunch collisions,  $n_b$  the number of proton per bunch,  
<sup>483</sup> and  $\sigma_x$  and  $\sigma_y$  are the horizontal and vertical dimensions of the beam. The luminosity is  
<sup>484</sup> strictly related to the number of collisions occurring during a certain experiment via the  
<sup>485</sup> following:

$$\mathcal{N}_{\text{event}} = \mathcal{L}\sigma_{\text{event}} \quad (2.2)$$

<sup>486</sup> where  $\sigma_{\text{event}}$  is the cross section of the process under investigation. It has not only collided  
<sup>487</sup> protons but also heavy ions, in particular lead nuclei at  $\sqrt{s_{NN}} = 5.02 \text{ TeV}$ , at a luminosity  
<sup>488</sup> of  $10^{27} \text{ cm}^{-2} \text{s}^{-1}$  [18].

#### <sup>489</sup> Acceleration stages

<sup>490</sup> Before reaching the maximum energy, the proton beams are accelerated by smaller ac-  
<sup>491</sup> celerators through various stages. Figure 2.1 shows a sketch of the CERN's accelerator  
<sup>492</sup> complex. It all begins at the linear accelerator LINAC 2. Here protons are accelerated up  
<sup>493</sup> to 50 MeV, and then injected in the Proton Synchrotron Booster (PSB) where they reach  
<sup>494</sup> 1.4 GeV. The next stage is the Proton Synchrotron (PS), which boosts the beams up to 25  
<sup>495</sup> GeV and then the Super Proton Synchrotron (SPS) makes them reach energies up to 450  
<sup>496</sup> GeV. Eventually, the beams are injected in bunches with a 25 ns spacing into the LHC,  
<sup>497</sup> where they travel in opposite directions, while they are accelerated to up to 13 TeV. Once

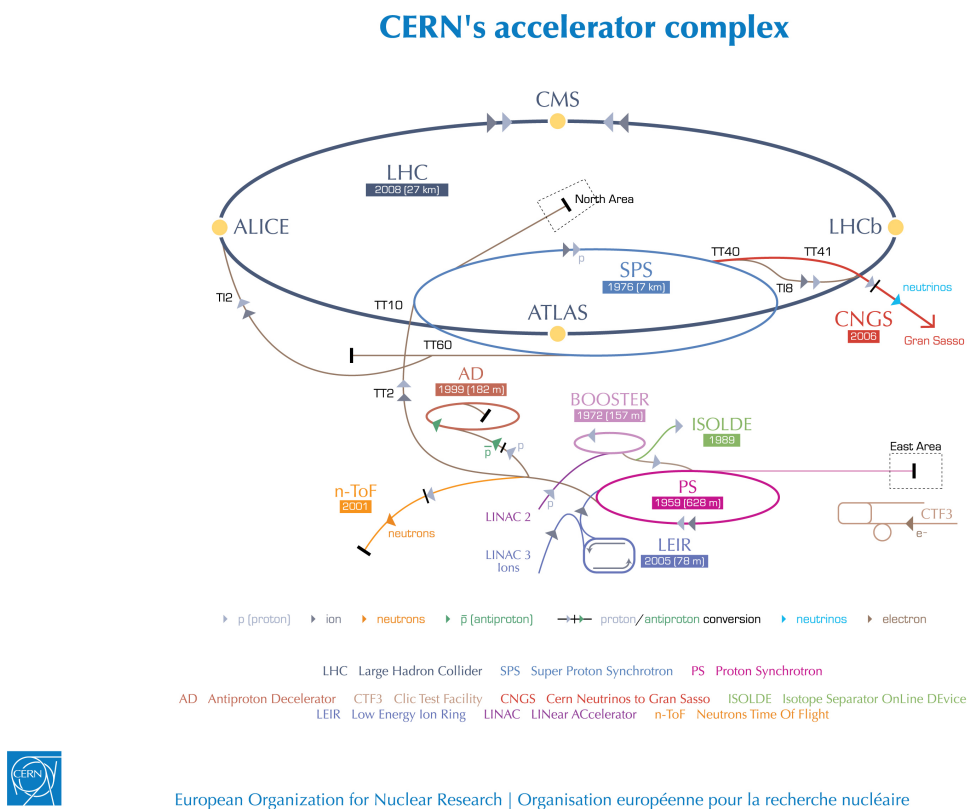


Figure 2.1: CERN Accelerator complex. The LHC is the last ring (dark grey line). Smaller machines are used for early-stage acceleration and also to provide beams for other experiments [3].

498 the bunches reach the maximum energy, they are made collide at four different points,  
 499 inside four experiments around the ring [19].

500 The heavy ion beams acceleration procedure is slightly different. Their journey starts  
 501 at LINAC 3 first, and the Low Energy Ion Ring (LEIR) then, before they make their way  
 502 into the PS where they follow the same path as the protons [19].

503 The four large detectors on the collision points are; the multi-purpose detectors A Tor-  
 504 oidal LHC ApparatuS (ATLAS), and Compact Muon Solenoid (CMS) [20], Large Hadron  
 505 Collider beauty (LHCb) [21], which focuses on flavour physics, and A Large Ion Collider  
 506 Experiment (ALICE) [22] which specialises in heavy ion physics. The *big four* are not the  
 507 only experiments at the CERN's accelerator complex. There also are smaller experiments  
 508 based at the the four caverns about the collision points e.g. TOTEM, LHCf and MoEDAL,  
 509 but this will not be discussed any further in this thesis.

## 510 2.2 The ATLAS Detector

511 ATLAS is a general-purpose detector designed to collect data with the highest luminosity  
 512 provided by the LHC. It is located at CERN's Point 1 cavern and it measures about 45 m in

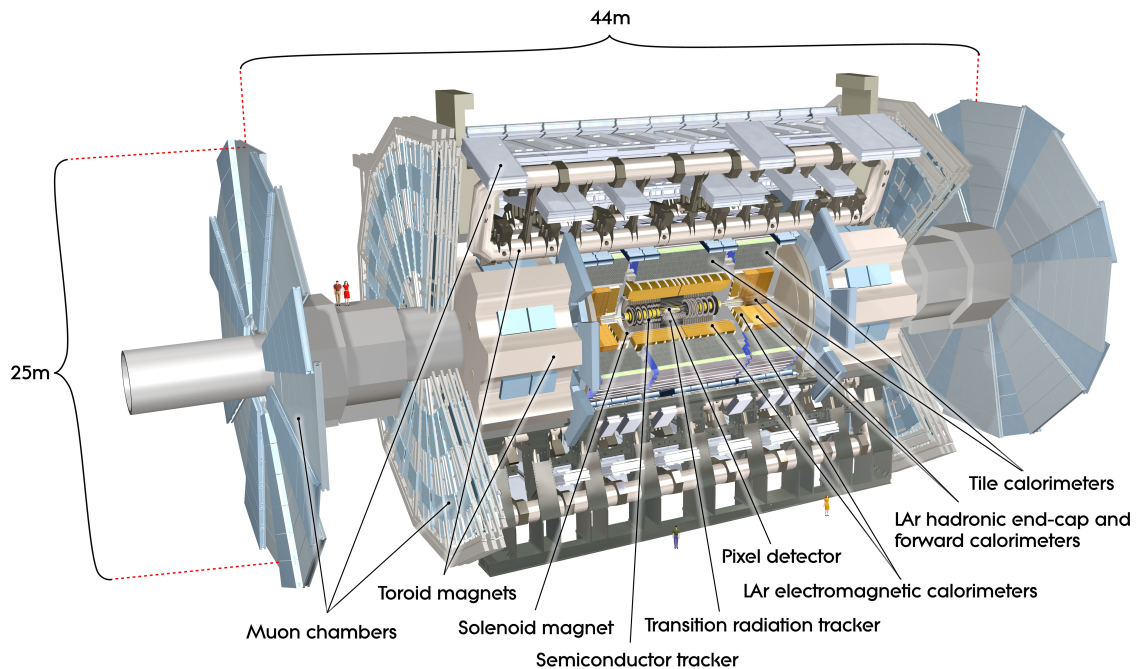


Figure 2.2: Cut-away view of the ATLAS detector. The dimensions of the detector are 25 m in height and 44 m in length. The overall weight of the detector is approximately 7000 tonnes [3].

length and 25 m in diameter. It has a forward-backward symmetric cylindrical geometry with respect to the interaction point and it is designed to reconstruct and measure physics objects such as electrons, muons, photons and hadronic jets. Its design was optimised to be as sensitive as possible to the discovery of the Higgs boson and beyond-the-Standard-Model (BSM) physics. In fact, thanks to the other sub-systems, ATLAS is able to observe all possible decay products by covering nearly  $4\pi$  steradians of solid angle.

In Figure 2.2 a cut-away view of ATLAS with all its components is shown. The inner-most layer is the Inner Detector (ID) which is the core of the tracking system and consists of a Pixel, a Silicon micro-strip tracker (SCT), and a Transition Radiation Tracker (TRT). It is submerged in a 2 T magnetic field, generated by a thin superconducting solenoid, which bends all the charged particles' trajectories allowing transverse momentum measurement. The electromagnetic and hadronic calorimeters form the next layer and they are both used to perform precise energy measurements of photons, electrons, and hadronic jets. Finally, the outermost layer corresponds to the Muon Spectrometer (MS) which, together with the ID, enclosed in a toroidal magnetic field, allows precise measurement of momentum and position of muons. These sub-detectors will be discussed in more detail in the following sections.

**530 The ATLAS coordinate system**

**531** A coordinate system is taken on for the spatial definition of the sub-systems and kinematic  
**532** measurement of physics processes. Such system is defined starting from the interaction  
**533** point, defined as the origin. The  $z$ -axis is defined by the beam direction and the  $x - y$   
**534** plan, as transverse to the beam direction.

**535** A quantity, known as pseudorapidity, ( $\eta$ ), is defined to describe the angle of a particle  
**536** coming out of the collision, with respect to the beam axis:

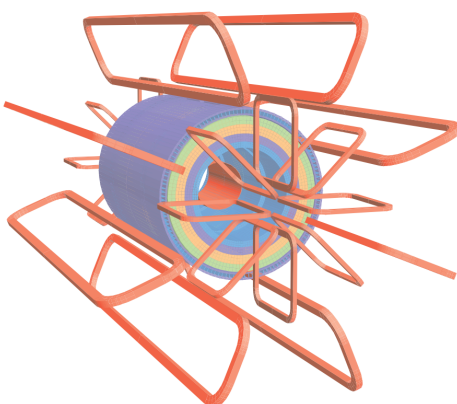
$$\eta \equiv -\ln(\tan(\theta/2))$$

**537** Here  $\theta$  is the polar angle. The azimuthal angle,  $\phi$ , is defined around the beam axis and  
**538** the polar angle. In the  $(\eta, \phi)$  space a distance  $\Delta R$  can be therefore defined as

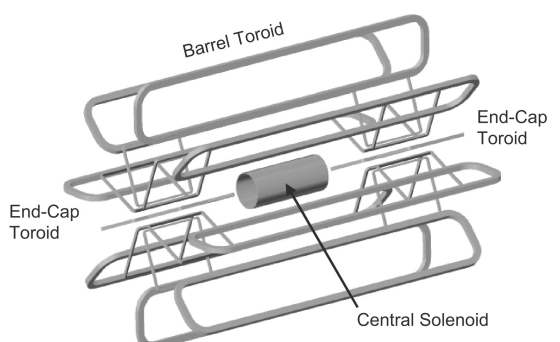
$$\Delta R = \sqrt{\Delta\eta^2 + \Delta\phi^2}$$

**539** where  $\Delta\eta$  and  $\Delta\phi$  are the differences in pseudorapidity and azimuthal angle between any  
**540** two considered objects. A central and a forward region of pseudorapidity are also defined  
**541** such that the detector components are described as part of the *barrel* if they belong to the  
**542** former or as part of the *end-caps* if they belong to the latter.

**543 2.2.1 The Magnet System**



(a) Geometry of magnet windings and tile calorimeter steel. The eight barrel toroid coils, with the end-cap coils interleaved are visible. The solenoid winding lies inside the calorimeter volume [4].



(b) Schematic view of the superconducting magnets [23].

Figure 2.3: The ATLAS magnet system.

544 The ATLAS magnet system, 26 m long with a 22 m diameter, generates the magnetic field  
 545 needed to bend the trajectories of charged particles in order to perform momentum meas-  
 546 urement. Figure 2.3a and 2.3b show the geometry of the system and its components,  
 547 which are made of NbTi - superconducting material - and will be described in the follow-  
 548 ing paragraphs.

### 549 **The Central Solenoid**

550 With an axial length of 5.8 m, an inner radius of 2.46 m, and an outer radius of 2.56 m, the  
 551 central solenoid magnet is located between the ID and the ECAL. Its function is to bend  
 552 the charged particles that go through the ID and it is aligned on the beam axis providing  
 553 a 2 T axial magnetic field that allows accurate momentum measurement up to 100 GeV  
 554 [23].

### 555 **The Barrel and the End-cap Toroids**

556 Figure 2.3b displays the toroid magnetic system that surrounds the calorimeters. With its  
 557 cylindrical shape this component consists of a barrel and two end-caps toroids, each with  
 558 eight superconducting coils. The system allows accurate measurement of muon momenta  
 559 using a magnetic field of approximately 0.5 T (barrel) for the central regions and 1 T (end-  
 560 cap) for the end-cap regions, respectively, which bends the particles in the  $\theta$  direction.

#### 561 **2.2.2 The Inner Detector**

562 The Inner Detector (ID) [24] is the innermost component of the ATLAS detector i. e. the  
 563 nearest sub-detector to the interaction region and it is used to reconstruct charged particle  
 564 tracks used in the selection of physics objects. In fact, it allows robust track reconstruction,  
 565 with accurate impact parameter resolution ( $\sim 20\mu m$ ) and precise primary and secondary  
 566 vertex reconstruction for charged particles (tracks) above 500 MeV and within  $|\eta| < 2.5$ .

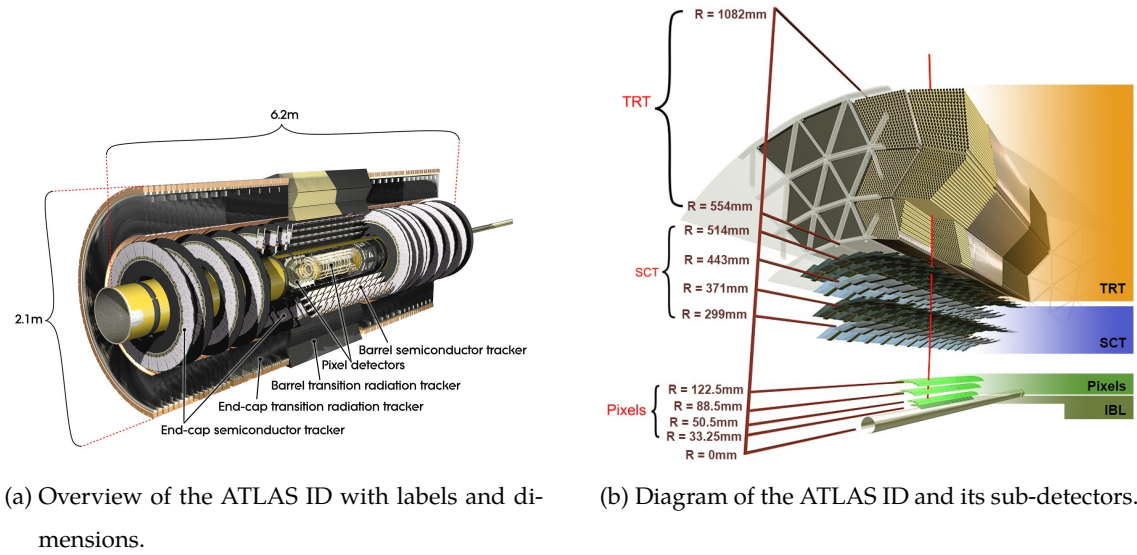
567 The ID is comprised of independent and concentric sub-systems, which are all shown  
 568 in Figure 2.4:

- 569     • Insertable B-Layer (IBL):

570       innermost Pixel Detector layer added during ATLAS Run 2 upgrade (2013/2014) to  
 571       improve vertexing and impact parameter reconstruction;

- 572     • Silicon Pixel Tracker (Pixel):

573       made of silicon pixel layers and used mainly for reconstructing both the primary



(a) Overview of the ATLAS ID with labels and dimensions.

(b) Diagram of the ATLAS ID and its sub-detectors.

Figure 2.4: The ATLAS Inner Detector

574 and secondary vertices in an event;

575 • SemiConductor Tracker (SCT):

576 comprised of silicon microstrip layers; thanks to its resolution ( $17 \times 580 \mu\text{m}$ ) it can  
577 accurately measure particle momenta;

578 • Transition Radiation Tracker (TRT):

579 final layer comprised of various layers of gaseous straw tube elements surrounded  
580 by transition radiation material.

581 These sub-detectors will be discussed in the following sections.

582 **IBL**

583 The IBL [25] is the innermost Pixel Detector layer as shown in Figure 2.4b. It is comprised  
584 of 6M channels and each pixel measures  $50 \times 250 \mu\text{m}$ . Its resolution is  $8 \times 40 \mu\text{m}$ ,The  
585 addition of this new layer brought a considerable improvement on the performance of the  
586 Pixel Detector by enhancing the quality of impact parameter reconstruction of tracks. In  
587 particular, this was achieved by improving the vertex finding efficiency and the tagging  
588 of bottom-quark-initiated jets ( $b$ -jets) which, in case of a B-layer failure, can be restored  
589 by the IBL. Besides these improvements, the IBL insertion allowed ATLAS to better cope  
590 with high luminosity effects such as the increase in event pile-up, which leads to high  
591 occupancy and read-out inefficiency.

---

## 592 Pixel

593 The Pixel detector is comprised of 1750 identical sensorchip-hybrid modules, each cover-  
 594 ing an active area of  $16.4 \times 60.8$  mm. The total number of modules correspond to roughly  
 595 80 million semiconductor silicon pixels. The nominal pixel size is  $50 \mu\text{m}$  in the  $\phi$  direction  
 596 and  $400 \mu\text{m}$  in the barrel region, along the  $z$ -axis (beam axis) [26]. The reason why such a  
 597 large amount of pixels is employed is justified by the need to cope with the high luminos-  
 598 ity in ATLAS. The silicon pixel detector measures 48.4 cm in diameter and 6.2 m in length  
 599 providing a pseudorapidity coverage of  $|\eta| < 2.5$ . Figure 2.4b shows the three concentric  
 600 barrel layers placed at 50.5 mm, 88.5 mm and 122.5 mm respectively. Furthermore, the  
 601 Pixel detector is made of six disk layers, three for each forward region, such that when a  
 602 charged particle crosses the layers it will generate a signal at least in three space points.  
 603 The fine granularity of such detector allows accurate measurement and precise vertex re-  
 604 construction, as it provides a more accurate position measurement as a large detection  
 605 area is available. In particular, it has a resolution of  $10 \times 115 \mu\text{m}$ .

## 606 SCT

607 The SCT is made of 4088 modules of silicon micro-strip detectors arranged in four con-  
 608 centric barrel layers. It is mainly used for precise momentum reconstruction over a range  
 609  $|\eta| < 2.5$  and it was designed for precision measurement of the position using four points  
 610 (corresponding to eight silicon layers), obtained as track hits when crossing the layers.  
 611 Figure 2.4b shows the structure of the SCT with its four concentric barrel layers with radii  
 612 ranging from 299 mm to 514 mm and two end-cap layers. Each module has an intrinsic  
 613 resolution of  $17 \mu\text{m}$  in the  $R - \phi$  direction and  $580 \mu\text{m}$  in the  $z$  direction. As the SCT is fur-  
 614 ther away from the beam-pipe than the Pixel detector, it has to cope with reduced particle  
 615 density. This allows for reduced granularity maintaining the same level of performance of  
 616 the Pixel detector: SCT can use  $\sim 6.3$  million read-out channels.

## 617 TRT

618 The last and outermost of the sub-systems in the ID is the TRT. It is a gaseous detector  
 619 which consists of 4 mm diameter straw tubes wound from a multilayer film reinforced  
 620 with carbon fibers and containing a  $30 \mu\text{m}$  gold plated tungsten wire in the center. The  
 621 straw is filled with a gas mixture of 70% Xe, 27% CO<sub>2</sub> and 3% O<sub>2</sub> [27]. As shown in Figure  
 622 2.4b, its section consists of three concentric layers with radii ranging from 544 mm to 1082  
 623 mm, each of which has 32 modules containing approximately 50,000 straws, 1.44 m in

---

length, aligned parallel to the beam direction with independent read-out at both ends.  
 Both end-cap sections are divided into 14 wheels, with roughly 320,000 straws in the R-direction. The average 36 hits per track in the central region of the TRT allow continuous tracking to enhance pattern recognition and momentum resolution in the  $|\eta| < 2.5$  region.  
 It also improves the  $p_T$  resolution for longer tracks.

### 2.2.3 The Calorimeters

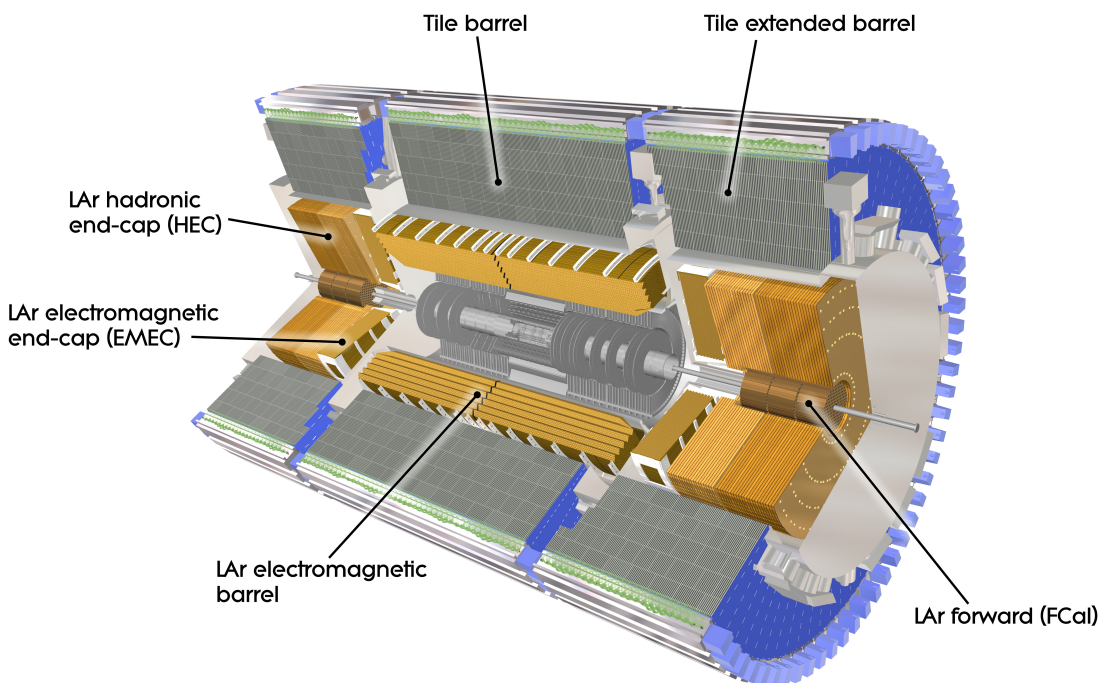


Figure 2.5: A computer generated image of the full calorimeter.

The ATLAS Calorimeter system, shown in Figure 2.5, is comprised of two main subsystems; the electromagnetic calorimeter (ECAL) and hadronic calorimeter (HCAL), which are designed to stop and measure the energy of electromagnetic-interacting and hadronic particles respectively. The combination of the two provides full coverage in  $\phi$  and  $|\eta| < 4.95$ . Particles slow down and lose energy generating showers when crossing different layers. The ECAL is comprised of one barrel and two end-cap sectors employing liquid Argon (LAr). The showers hereby develop as electrons pairs which are then collected. The HCAL is also comprised of one barrel and two end-cap sectors. The sensors in the barrel of the HCAL are tiles of scintillating plastic whereas LAr is employed for the end-cap. A forward region, the closest possible to the beam, is covered by a LAr forward calorimeter (FCal). The LAr and Tile Calorimeter will be briefly discussed in the

641 following paragraphs.

## 642 The Liquid Argon Calorimeters

643 The ECAL is comprised of multiple layers of liquid Argon (LAr) sampler and lead ab-  
 644 sorber. The choice of its accordion-geometry design brought two main advantages; full  
 645  $\phi$  coverage with no non-interactive regions (no cracks); fast extraction of signals coming  
 646 from both front or rear end of the electrodes. It is made of two half-barrel wheels, both  
 647 placed in the barrel cryostat, that provide a pseudorapidity coverage up to  $|\eta| < 1.475$   
 648 and two end-cap detectors providing  $1.375 \leq |\eta| \leq 3.20$  coverage in two end-cap cryo-  
 649 stats. The junction between the barrel and end cap components defines the crack region  
 650 and any signal coming from the crack region is therefore discarded.

651 In the  $|\eta| < 1.8$  region there is an additional layer, placed at the front of the calorimeter,  
 652 that is made of a thin (0.5 cm in the end-cap and 1.1 cm in the barrel) LAr layer with  
 653 no absorber [28]. This additional layer was designed to correct for the energy lost, as  
 654 particles enter the calorimeter, by taking a measurement just before the majority of the  
 655 electromagnetic shower is developed.

## 656 The Tile calorimeter

657 The main purpose of the hadronic calorimeter is to measure the energy of hadronic showers.  
 658 It is built employing steel and scintillating tiles coupled to optical fibres which are read  
 659 out by photo-multipliers. As shown in Figure 2.5, the HCAL is made up of three cylin-  
 660 ders; a central barrel, 5.64 m long covering a region  $|\eta| < 1.0$ , and two extended barrel,  
 661 2.91 m long covering a reigon  $0.8 < |\eta| < 1.7$ . Each cylinder is made up of 64 modules  
 662 and each module is in turn made up of three layers. Ultimately, the smallest section of the  
 663 calorimeter module is a cell with a  $\Delta\phi \times \Delta\eta = 0.1 \times 0.1$  granularity for the two innermost  
 664 layers and  $\Delta\phi \times \Delta\eta = 0.2 \times 0.1$  for the outermost one.

### 665 2.2.4 The Muon Spectrometer

666 The MS [29], shown in Figure 2.6, is the outermost sub-system of the whole ATLAS de-  
 667 tector. As such, it surrounds the calorimeters and its main function is to perform precision  
 668 measurement of muons momenta. The deflection of muon tracks employing large super-  
 669 conducting air-core toroid magnets and high-precision tracking chambers is at the heart  
 670 of such high precision measurement.

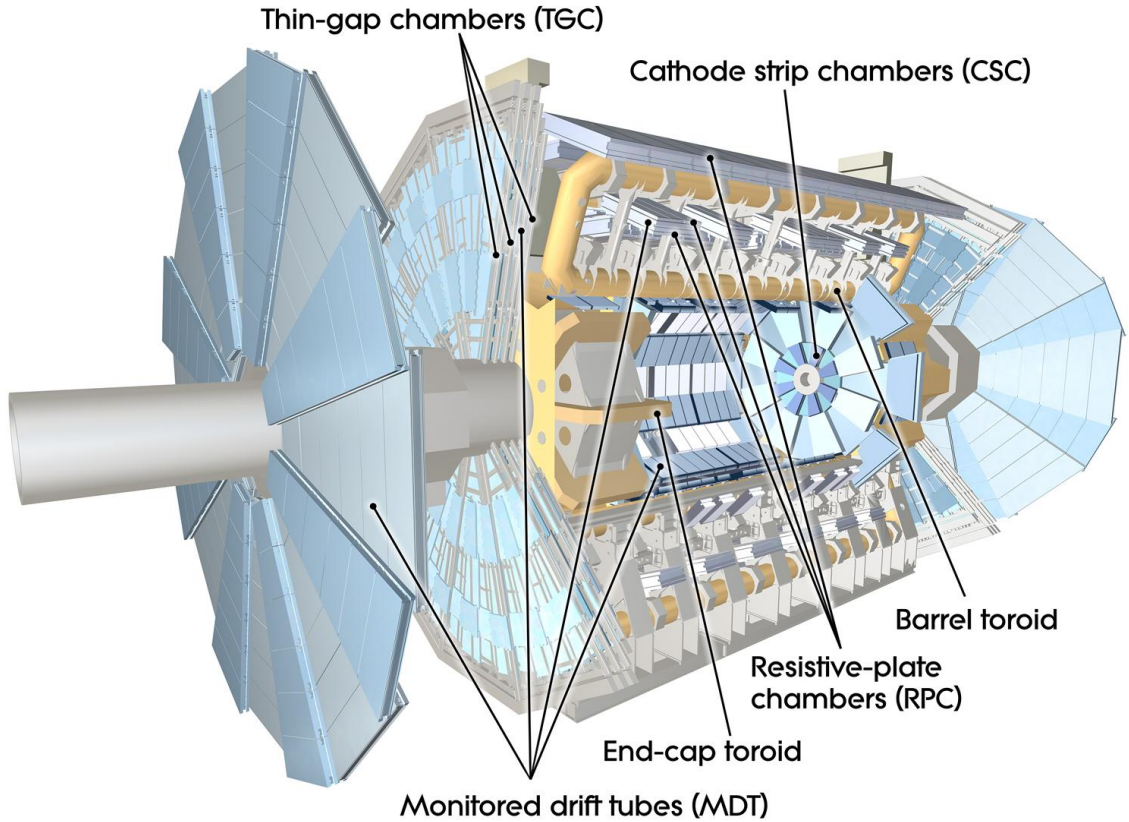


Figure 2.6: Cut-away view of the ATLAS muon system [4].

671        The MS is comprised of one large barrel toroid, covering the region  $|\eta| \leq 1.4$ , and  
 672        two end-cap toroids, covering  $1.6 < |\eta| \leq 2.7$  which are employed together to achieve the  
 673        track-bending effect wanted. The magnitude of the magnetic field in the barrel, generated  
 674        by eight large superconducting coils, ranges from 0.5 to 2 T.

675        Around the beam axis, three cylindrical layers make way for the chambers, placed in  
 676        planes perpendicular to the beam, used to measure tracks.

677        Monitored Drift Chambers (MDTs) are employed over most of the pseudorapidity  
 678        range to provide precision measurement of track coordinates in the bending direction.  
 679        Cathode Strip Chambers (CSCs) are instead employed at large pseudorapidity ( $2 < |\eta| <$   
 680        2.7). Finally, in the end-cap regions Thin-Gap Chambers (TGCs) together with Resistive-  
 681        Plate Chambers (RPCs) are dedicated to the Trigger System discussed in Section 2.3.

## 682 2.3 The ATLAS Trigger System

683        The ATLAS Trigger System is at the heart of data taking. It is an essential component of  
 684        any nuclear or particle physics experiment since it is responsible for deciding whether or  
 685        not to store an event for later study [5]. The ATLAS Trigger system is employed to reduce

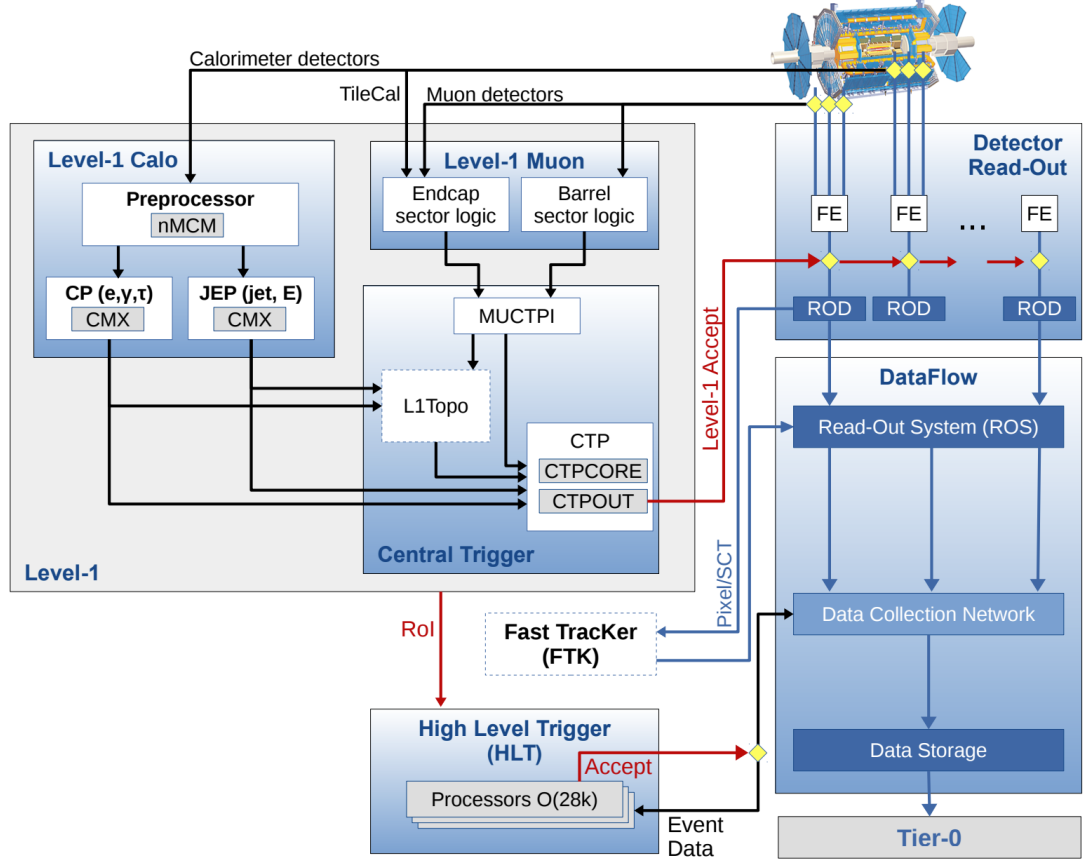


Figure 2.7: The ATLAS TDAQ system. L1Topo and FTK were being commissioned during 2015 and not used for the results shown in this thesis [5].

686 the event rate from  $\sim 40 \text{ MHz}$ <sup>1</sup> bunch-crossing<sup>2</sup> to  $\sim 200 \text{ Hz}$  which corresponds to roughly  
687  $300 \text{ MB/s}$ .

688 The Trigger and Data Acquisition (TDAQ) system shown in Figure 2.7 consists of a  
689 hardware-based first level trigger (L1) and a software-based high-level trigger (HLT). The  
690 L1 trigger decision is formed by the Central Trigger Processor (CTP), which receives in-  
691 puts from the L1 calorimeter (L1Calo) and L1 muon (L1Muon) triggers. The first level  
692 (L1), which was designed to perform the first selection step, is a hardware-based system  
693 that uses information from the calorimeter and muon subdetectors. It also defines the  
694 so-called Regions of Interest (RoIs) within the detector to be investigated by the next level  
695 trigger, the HLT. Additionally, a Fast TracKer (FTK) system [30] (not yet installed) will  
696 provide global ID track reconstruction at the L1 trigger rate using lookup tables stored in

<sup>1</sup>The LHC delivers beams with a bunch-spacing of 25 ns.

<sup>2</sup>The term bunch-crossing is hereby used when referring to a collision between two bunches of protons. Since only a certain fraction of the total momentum carried by each proton contributes to the collision, an average number of interactions per bunch-crossing,  $\langle \mu \rangle$  is used.

<sup>697</sup> custom associative memory chips for the pattern recognition. The FPGA-based track fitter  
<sup>698</sup> will perform a fast linear fit and the tracks are made available to the HLT. This system will  
<sup>699</sup> allow the use of tracks at much higher event rates in the HLT than is currently affordable  
<sup>700</sup> using CPU systems. However, the upgrade of the ATLAS trigger will not be discussed  
<sup>701</sup> any further.

<sup>702</sup> In the next sections the L1 and HLT will be briefly described.

### <sup>703</sup> 2.3.1 Level 1 Trigger

<sup>704</sup> The Level 1 Trigger identifies Regions of Interest (RoIs)<sup>3</sup> and passes these to HLT which  
<sup>705</sup> will perform further investigations. Furthermore, in order to decide whether or not the  
<sup>706</sup> event processing will continue, L1 selection uses only information coming from some  
<sup>707</sup> parts of the detector to keep the input rate to a maximum of 100 kHz. L1 is implemented  
<sup>708</sup> in fast custom electronics to keep the latency<sup>4</sup> below 2.5  $\mu$ s. Event data from other sub-  
<sup>709</sup> syststem are temporarily stored in memories whilst L1 decision is taken.

<sup>710</sup> The L1 topological trigger (L1-Topo) [31] is feeded with energy and direction inform-  
<sup>711</sup> ation, about the objects found by the L1 calorimeter and the muon trigger, which will be  
<sup>712</sup> processed by dedicated algorithms implemented in its own FPGAs. However, due to the  
<sup>713</sup> 100 kHz read-out rate, not all the information collected by L1-Topo will be sent to the HLT,  
<sup>714</sup> but only part of it. In order to properly seed the ROI-guided HLT reconstruction, specific  
<sup>715</sup> objects in combination with the correct topological criteria must be employed.

### <sup>716</sup> 2.3.2 High-Level Trigger

<sup>717</sup> The HLT is used to reduce the output rate down to 1 kHz and it has a  $\sim$ 200 ms average  
<sup>718</sup> decision time. Events that pass L1 trigger are then processed by the HLT using finer-  
<sup>719</sup> granularity calorimeter information, precision measurements from the MS and tracking  
<sup>720</sup> information from the ID. The HLT reconstruction can be run within RoIs identified at L1  
<sup>721</sup> or a so-called full-scan on the full detector can be performed. The track reconstruction in  
<sup>722</sup> the Inner Detector is an essential component of the trigger decision in the HLT and it will  
<sup>723</sup> be discussed more in detail in Chapter 3

---

<sup>3</sup> $\eta - \phi$  regions where event features have been found by the L1 selection process.

<sup>4</sup>Time needed by an electric signal to get to the front-end electronics.

724 **3** | The *b*-jet Trigger Signature in AT-  
725 LAS

726 In this chapter the monitor and performance of the bottom-quark-initiated jet (*b*-jet) sig-  
727 nature trigger, this being the author’s “technical/qualification task” to become a qualified  
728 member of the experiment, will be discussed. The efficiencies of some of the Run 2 *b*-jet  
729 triggers were evaluated using  $3.8 \text{ fb}^{-1}$  of  $pp$  collisions data collected in 2015 with 25 ns  
730 bunch-spacing.

731 The qualification task

732 **3.1 Trigger Efficiency**

# 733 4 | Event Simulation and Reconstruction

734

735 bla bla bla

## 736 4.1 Event Generation

737 bla bla

### 738 4.1.1 Parton Distribution Functions (PDFs)

739 bla bla bla

### 740 4.1.2 Matrix Element Calculation

741 bla bla bla

### 742 4.1.3 Parton Showers

743 bla bla bla

### 744 4.1.4 Hadronisation

745 bla bla bla

## 746 4.2 Detector Simulation

747 bla bla bla

748    **5** | Stop searches in final states with  
749    jets and missing transverse en-  
750    ergy

<sup>751</sup> **6** | Results and Statistical Interpretations

<sup>752</sup>

<sup>753</sup> Trigger

<sup>754</sup> bla vlas bla

# Bibliography

- [1] ATLAS Collaboration, "Summary plots from the atlas standard model physics group." [https://atlas.web.cern.ch/Atlas/GROUPS/PHYSICS/CombinedSummaryPlots/SM/ATLAS\\_a\\_SMSummary\\_TotalXsect/ATLAS\\_a\\_SMSummary\\_TotalXsect.png](https://atlas.web.cern.ch/Atlas/GROUPS/PHYSICS/CombinedSummaryPlots/SM/ATLAS_a_SMSummary_TotalXsect/ATLAS_a_SMSummary_TotalXsect.png). viii, 9
- [2] C. Borschensky, M. Krämer, A. Kulesza, M. Mangano, S. Padhi, T. Plehn, and X. Portell, *Squark and gluino production cross sections in pp collisions at  $\sqrt{s} = 13, 14, 33$  and 100 TeV*, *Eur. Phys. J.* **C74** no. 12, (2014) 3174, [arXiv:1407.5066 \[hep-ph\]](https://arxiv.org/abs/1407.5066). viii, 16
- [3] C. Lefèvre, *The CERN accelerator complex*, <http://cds.cern.ch/record/1260465>. viii, 20, 21
- [4] ATLAS Collaboration, *The ATLAS experiment at the CERN Large Hadron Collider*, *Journal of Instrumentation* **3** no. 08, (2008) S08003. <http://stacks.iop.org/1748-0221/3/i=08/a=S08003>. ix, 22, 28
- [5] A. Collaboration, *Performance of the ATLAS Trigger System in 2015*, *Eur. Phys. J.* **C77** (2017), [arXiv:1611.09661 \[hep-ex\]](https://arxiv.org/abs/1611.09661). ix, 28, 29
- [6] M. Herrero, *The Standard Model*, <https://arxiv.org/abs/hep-ph/9812242>. 2
- [7] ATLAS Collaboration, *Observation of a New Particle in the Search for the Standard Model Higgs Boson with the ATLAS Detector at the LHC*, *Phys.Lett.* **B716** (2012), [arXiv:1207.7214 \[hep-ex\]](https://arxiv.org/abs/1207.7214). 2
- [8] CMS Collaboration, *Observation of a new boson at a mass of 125 GeV with the CMS experiment at the LHC*, *Phys.Lett.* **B716** (2012), [arXiv:1207.7235 \[hep-ex\]](https://arxiv.org/abs/1207.7235). 2
- [9] A. Pich, *The Standard Model of Electroweak Interactions*, [arXiv:1201.0537 \[hep-ph\]](https://arxiv.org/abs/1201.0537). 5, 6

- 779 [10] K. A. Olive at al. (Particle Data Group), *Review of Particle Physics*, **Chin.Phys. C** **38(9)**  
 780 (2014). 6
- 781 [11] J. Goldstone, A. Salam and S. Weinberg, *Broken Symmetries*, **Phys. Rev.** **127** (1962)  
 782 965–970. 8
- 783 [12] S. Weinberg, *Implications of Dynamical Symmetry Breaking*, **Phys. Rev.** **D19** (1976)  
 784 1277–1280. 10
- 785 [13] Super-Kamiokande Collaboration, Y. Fukuda et al., *Evidence for oscillation of*  
 786 *atmospheric neutrinos*, **Phys. Rev. Lett.** **81** (1998) 1562–1567, [arXiv:hep-ex/9807003](https://arxiv.org/abs/hep-ex/9807003)  
 787 [[hep-ex](#)]. 10
- 788 [14] SNO Collaboration, *Measurement of the Rate of  $\nu_e + d \rightarrow p + p + e^-$  Interactions*  
 789 *Produced by  ${}^8B$  Solar Neutrinos at the Sudbury Neutrino Observatory*, **Phys. Rev. Lett.**  
 790 **87** (2001). 10
- 791 [15] T. O. W. of the Nobel Prize.  
 792 [https://www.nobelprize.org/nobel\\_prizes/physics/laureates/2015/](https://www.nobelprize.org/nobel_prizes/physics/laureates/2015/). 10
- 793 [16] F. Jegerlehner, *The hierarchy problem of the electroweak Standard Model revisited*,  
 794 [arXiv:1305.6652](https://arxiv.org/abs/1305.6652) [[hep-ph](#)]. 12
- 795 [17] Johan Alwall, Philip C. Schuster and Natalia Toro, *Simplified models for a first*  
 796 *characterization of new physics at the LHC*, **Phys. Rev. D** **D79** (2009). 16
- 797 [18] J.M. Jowett, M. Schaumann, R. Alemany, R. Bruce, M. Giovannozzi, P. Hermes, W.  
 798 Hofle, M. Lamont, T. Mertens, S. Redaelli, J. Uythoven, J. Wenninger, *The 2015*  
 799 *Heavy-Ion Run of the LHC*,  
 800 <http://accelconf.web.cern.ch/accelconf/ipac2016/papers/tupmw027.pdf>. 19
- 801 [19] O. S. Brüuning, P. Collier, P. Lebrun, S. Myers, R. Ostojic, J. Poole and P. Proudlock,  
 802 *LHC Design Report*, <https://cds.cern.ch/record/782076>. 20
- 803 [20] CMS Collaboration, *The CMS experiment at the CERN LHC*, **Journal of**  
 804 **Instrumentation** **3** no. 08, (2008) S08004.  
 805 <http://stacks.iop.org/1748-0221/3/i=08/a=S08004>. 20
- 806 [21] LHCb Collaboration, et. al, *The LHCb Detector at the LHC*, **JINST** (2008). 20

- 807 [22] ALICE Collaboration, *The ALICE experiment at the CERN LHC*, Journal of  
808 Instrumentation **3** no. 08, (2008) S08002.  
809 <http://stacks.iop.org/1748-0221/3/i=08/a=S08002>. 20
- 810 [23] A. Yamamoto, Y. Makida, R. Ruber, Y. Doi, T. Haruyama, F. Haug, H. ten Kate,  
811 M. Kawai, T. Kondo, Y. Kondo, J. Metselaar, S. Mizumaki, G. Olesen, O. Pavlov,  
812 S. Ravat, E. Sbrissa, K. Tanaka, T. Taylor, and H. Yamaoka, *The ATLAS central*  
813 *solenoid*, Nuclear Instruments and Methods in Physics Research Section A:  
814 Accelerators, Spectrometers, Detectors and Associated Equipment **584** no. 1, (2008)  
815 53 – 74.  
816 <http://www.sciencedirect.com/science/article/pii/S0168900207020414>. 22,  
817 23
- 818 [24] ATLAS Collaboration, *The ATLAS Inner Detector commissioning and calibration*, Eur.  
819 Phys. JC**70** , [arXiv:1004.5293](https://arxiv.org/abs/1004.5293). 23
- 820 [25] ATLAS Collaboration, *ATLAS Insertable B-Layer Technical Design Report*,  
821 <https://cds.cern.ch/record/1291633>. 24
- 822 [26] G. A. et al., *ATLAS pixel detector electronics and sensors*, Journal of Instrumentation **3**  
823 no. 07, (2008) P07007. <http://stacks.iop.org/1748-0221/3/i=07/a=P07007>. 25
- 824 [27] A. Bingül, *The ATLAS TRT and its Performance at LHC*, Journal of Physics:  
825 Conference Series **347** no. 1, (2012) 012025.  
826 <http://iopscience.iop.org/article/10.1088/1742-6596/347/1/012025/meta>.  
827 25
- 828 [28] ATLAS Collaboration, *ATLAS liquid-argon calorimeter: Technical Design Report*,  
829 <https://cds.cern.ch/record/331061>. 27
- 830 [29] ATLAS Collaboration, *ATLAS muon spectrometer: Technical design report*,  
831 <https://cds.cern.ch/record/331068>. 27
- 832 [30] ATLAS Collaboration, *Fast TracKer (FTK) Technical Design Report*,  
833 <https://cds.cern.ch/record/1552953>. 29
- 834 [31] E. Simoni, *The Topological Processor for the future ATLAS Level-1 Trigger: from design to*  
835 *commissioning*, [arXiv:1406.4316](https://arxiv.org/abs/1406.4316). 30